



UNIVERSITÀ DI PARMA

ARCHIVIO DELLA RICERCA

University of Parma Research Repository

Joint identification of contaminant source and aquifer geometry in a sandbox experiment with the restart ensemble Kalman filter

This is a pre print version of the following article:

Original

Joint identification of contaminant source and aquifer geometry in a sandbox experiment with the restart ensemble Kalman filter / Chen, Zi; Gómez-Hernández, J. Jaime; Xu, Teng; Zanini, Andrea. - In: JOURNAL OF HYDROLOGY. - ISSN 0022-1694. - 564:(2018), pp. 1074-1084. [10.1016/j.jhydrol.2018.07.073]

Availability:

This version is available at: 11381/2849062 since: 2018-10-11T10:10:25Z

Publisher:

Elsevier B.V.

Published

DOI:10.1016/j.jhydrol.2018.07.073

Terms of use:

Anyone can freely access the full text of works made available as "Open Access". Works made available

Publisher copyright

note finali coverage

(Article begins on next page)

Joint identification of contaminant source and aquifer geometry in a sandbox experiment with the restart Ensemble Kalman filter

Zi Chen^a, J. Jaime Gómez-Hernández^a, Teng Xu^{a,*}, Andrea Zanini^b

^a*Institute of Water and Environmental Engineering, Universitat Politècnica de València, Valencia, Spain*

^b*Dipartimento di Ingegneria e Architettura, Università degli Studi di Parma, Parma, Italy*

Abstract

Contaminant source identification is a key problem in handling groundwater pollution events. The ensemble Kalman filter (EnKF) is used for the spatiotemporal identification of a point contaminant source in a sandbox experiment, together with the identification of the position and length of a vertical plate inserted in the sandbox that modifies the geometry of the system. For the identification of the different parameters, observations in time of solute concentration are used, but not of piezometric head data since they were not available. A restart version of the EnKF is utilized because it is necessary to restart the forecast from time zero after each parameter update. The results show that the restart EnKF is capable of identifying both contaminant source information and aquifer-geometry-related parameters together with an uncertainty estimate of such identification.

Keywords: Inverse modeling; Observation error; Groundwater laboratory experiment; Stochastic hydrogeology

1. Introduction

2 The problem of identifying a contaminant source in an aquifer using solute concentra-
3 tion data has been the subject of attention for many years (e.g., Atmadja and Bagtzoglou,

*Corresponding author

Email address: tenxu@posgrado.upv.es (Teng Xu)

4 2001; Michalak and Kitanidis, 2004; Bagtzoglou and Atmadja, 2005; Sun et al., 2006, and
5 references therein). Briefly, the proposed methods could be grouped into two categories:
6 optimization approaches and probabilistic approaches. The main difference between the two
7 approaches is that the optimization approaches cast the problem as a deterministic one in
8 which parameters are found that minimize a given objective function, whereas the probabilis-
9 tic approaches cast the problem in a stochastic framework and the parameters to estimate
10 become random variables. In the first category, Gorelick et al. (1983) identified the ground-
11 water pollution source information through an optimization model using linear programming
12 and multiple regression; Wagner (1992) employed a non-linear maximum likelihood method
13 to estimate source location and flux; Mahar and Datta (2000) used a nonlinear optimization
14 model for estimating the magnitude, location and duration of groundwater pollution sources
15 with binding equality constraints; Yeh et al. (2007) developed a hybrid approach, which
16 combines simulated annealing, tabu search and a three-dimensional groundwater flow and
17 solute transport model to solve the source identification problem; and Ayvaz (2010) utilized
18 a harmony search-based simulation-optimization model to determine the source location and
19 release histories by using an implicit solution procedure. In the second category, Bagtzoglou
20 et al. (1992) applied a particle method to estimate, probabilistically, source location and
21 spill-time history; Woodbury and Ulrych (1996) used a minimum relative entropy approach
22 to recover the release and evolution histories of a groundwater contaminant plume in a one-
23 dimensional system; Neupauer and Wilson (1999) employed a backward location model based
24 on adjoint state method (BPM-ASM) to identify a contaminant source; Butera et al. (2013)
25 utilized a simultaneous release function and source location identification (SRSI) method to
26 identify the release history and source location of an injection in a groundwater aquifer; and
27 Koch and Nowak (2016) derived and applied a Bayesian reverse-inverse methodology to infer
28 source zone architectures and aquifer parameters.

29 The ensemble Kalman filter (EnKF), which could be included in the group of probabilistic
30 approaches mentioned above, has recently addressed the problem of contaminant source

31 identification. The EnKF introduced by Evensen (2003) has gained much popularity in recent
32 years for its efficiency in solving inverse problems in different fields such as oceanography,
33 meteorology and hydrology (Houtekamer and Mitchell, 2001; Li et al., 2012a; Xu et al.,
34 2013b). The advantages of the EnKF can be summarized as follows (Chen and Zhang, 2006;
35 Zhou et al., 2011): computational efficiency when compared with other inverse approaches,
36 easy integration with different forecast models, ability to account for model and observation
37 errors, and easy uncertainty characterization since the final outcome is always an ensemble
38 of realizations. In hydrogeology, the EnKF has been mainly applied for the identification of
39 aquifer parameters such as hydraulic conductivity or porosity (Li et al., 2012b; Xu et al.,
40 2013a; Zhou et al., 2014; Xu and Gómez-Hernández, 2015, 2016a). Recently, Xu and Gómez-
41 Hernández (2016b) demonstrated the possibility to apply the EnKF for the identification of a
42 contaminant source in a deterministic synthetic aquifer, and later Xu and Gómez-Hernández
43 (2018) showed that the method can be also applied for the simultaneous identification of
44 hydraulic conductivities and the parameters defining a contaminant source also in a synthetic
45 aquifer.

46 All the works mentioned above were tested in synthetic cases. Only a few works can be
47 found in the literature for laboratory or field cases. Woodbury et al. (1998) extended the
48 minimum relative entropy (MRE) method to recover the release history of a contaminant and
49 applied it to reconstruct the release history of a 1,4-dioxane plume observed at the Gloucester
50 Landfill in Ontario, Canada. Michalak (2003); Michalak and Kitanidis (2004) employed a
51 Bayesian inverse formulation to estimate the contaminant history of trichloroethylene (TCE)
52 and perchloroethylene (PCE) in an aquifer at the Dover Air Force Base, Delaware, a site that
53 had already been analyzed by Liu and Ball (1999) in the same context of source identifica-
54 tion. Cupola et al. (2015b,a) compared the source location identification (SRSI) method to
55 the backward probability model based on the adjoint state method (BPM-ASM) with data
56 taken from a sandbox experiment. Zanini and Woodbury (2016) also used data from a sand-
57 box experiment to apply an empirical Bayesian method combined with Akaike's Bayesian

58 Information Criterion (ABIC) to deduce the release history of a groundwater contaminant.

59 The main objective of this paper is to assess the performance of the restart EnKF (r-
60 EnKF) for the identification of contaminant source parameters and aquifer geometry with
61 data from a sandbox experiment. The source parameters of interest are the release location,
62 release starting and ending times, and contaminant load, and regarding the geometry the
63 method should try to retrieve the position and length of a plate that is inserted about the
64 center of the sandbox and induces a deflection of the flowlines towards the bottom of the
65 sandbox. The state information assimilated by the r-EnKF is limited to concentration data
66 at a few observation points, since no piezometric head data were available.

67 The paper is organized as follows, first, the state equations and the fundamentals of the
68 r-EnKF will be recalled, second, the sandbox characteristics are described together with the
69 numerical model used to reproduce its behavior, third, the r-EnKF is tested with data from
70 a synthetic experiment that mimics the sandbox experiment with the aim to verify if the r-
71 EnKF is capable of identifying the kind of parameters sought, and four, the r-EnKF is applied
72 with observation values taken from the sandbox experiment, the problems encountered are
73 analyzed, alternative approaches are discussed and the final results presented. The paper
74 ends with a summary and conclusions on the main findings.

75 **2. Methodology**

76 *2.1. Groundwater Flow and Solute Transport Equation*

77 The sandbox will be modeled as a two-dimensional system in the XZ plane, where an
78 inert contaminant spreads due to advection and dispersion under a steady-state flow. The
79 dimension of the sandbox in the y direction is small enough to assume that the state variables
80 are constant along any line for any given (x, z) value. The governing equations are:

$$\frac{\partial}{\partial x} \left(K_x \frac{\partial h}{\partial x} \right) + \frac{\partial}{\partial z} \left(K_z \frac{\partial h}{\partial z} \right) + w = 0 \quad (1)$$

$$\frac{\partial(\theta C)}{\partial t} = \nabla \cdot (\theta D \cdot \nabla C) - \nabla \cdot (\theta v C) - q_s C_s \quad (2)$$

81 where K_x and K_z are the principal components of the hydraulic conductivity tensor in the x
 82 and z spatial coordinates respectively [LT^{-1}] which are assumed aligned with the coordinate
 83 system of reference in the entire domain; h is the hydraulic head [L]; w represents distributed
 84 sources or sinks [T^{-1}]; t is time [T]; θ represents the porosity of the medium; C is dissolved
 85 concentration [ML^{-3}]; $\nabla \cdot$ is the divergence operator; ∇ is the gradient operator; D represents
 86 the hydrodynamic dispersion coefficient tensor [L^2T^{-1}]; v is the flow velocity vector [LT^{-1}]
 87 derived from the solution of the flow model; q_s represents volumetric flow rate per unit
 88 volume of aquifer associated with a fluid source or sink [T^{-1}] and C_s is the concentration of
 89 the source or sink [ML^{-3}].

90 The flow equation is solved using MODFLOW (McDonald and Harbaugh, 1988), and the
 91 transport equation is solved using MT3DS (Zheng and Wang, 1999).

92 2.2. The Ensemble Kalman Filter

93 The ensemble Kalman filter was first introduced by Evensen (2003) to circumvent the
 94 difficulty of propagating covariances in time in the original and extended Kalman filter
 95 formulations. The restart EnKF (r-EnKF) has proven its capacity for contaminant source
 96 identification in synthetic cases (Xu and Gómez-Hernández, 2016b, 2018); now, we propose
 97 to test the r-EnKF in a sandbox experiment. For this specific case, there will be eight
 98 parameters to identify, six related to the contaminant source, and two related to aquifer
 99 geometry. In the first group, they are the contaminant source location (X_s, Z_s), the injection
 100 concentration I_c , the injection rate I_r , plus the starting T_s and ending T_e release times. In
 101 the second group, the algorithm will try to identify the position along the x direction X_b
 102 and the total depth Z_b of a vertical plate inserted about the center of the sandbox to deflect
 103 the flowlines. The rest of the parameters defining the flow and transport conditions in the
 104 sandbox are not subject to identification and are equal to their observed values as explained

105 in the description of the experiment in the next section. The r-EnKF is shortly described
106 next.

107 In the ensemble Kalman filter with extended state vector, we deal with two types of
108 variables, the system parameters subject of identification, of which there could be observa-
109 tions or not, and the state of the system, of which there will be observations. The state
110 is forecasted in time solving the corresponding state equations, with the latest parameter
111 update, up to the specific time steps when observations are collected; these observations are
112 assimilated by the filter and serve to update the parameters and the state of the system.
113 In the restart filter, state variables are not updated, only system parameters are, because
114 the system state forecast for the next observation time is restarted from time zero to make
115 sure that the forecasted system state is fully coherent with the state equations, and, in
116 our case, with the updated contaminant source. (In the original implementation of the fil-
117 ter, both state and parameters are updated, and the state system is forecasted from the
118 last updated state values using the last updated parameters.) The r-EnKF is an iterative
119 algorithm that cycles forecast and data assimilation (with the corresponding parameter up-
120 date) until all observations have been accounted for. The implementation of the r-EnKF
121 for the identification of the eight parameters described above can be summarized as follows
122 (Evensen, 2003; Xu and Gómez-Hernández, 2016b):

- 123 1. Generate an initial ensemble of parameter values. An ensemble of N_e realizations
124 of eight-tuples of the parameters to be identified is generated. Parameter values are
125 drawn, independently, from uniform distributions defined between first-guess minimum
126 and maximum values—there are no restrictions on these uniform distributions, their
127 range can be wider or narrower than the one used in this paper, and they do not have
128 to necessarily contain the “real” value, they are simply used to initialize the algorithm.
129 We build N_e vectors S_i with the eight parameters for each realization:

$$S_i = [Xs_i, Zs_i, Xb_i, Zb_i, Ic_i, Ir_i, Ts_i, Te_i]^T \quad (3)$$

130 where i is the realization index and the superscript T stands for transpose.

- 131 2. Repeat for each system state observation time. Forecast the state. For each ensemble
 132 member, forecast the system state, that is, the concentrations in the aquifer, for the
 133 t^{th} observation time using the values of the parameters from the last update (or the
 134 initial parameters for the first observation time). In the original implementation of
 135 the EnKF, the system state at the t^{th} observation time is forecasted based on the
 136 concentrations at the $(t-1)^{th}$ observation time and using the last updated parameters;
 137 however, it is virtually impossible to account for an update of the source location or
 138 the injection time unless the state equation is solved from time zero, thus the need to
 139 restart the simulation from time zero (Xu and Gómez-Hernández, 2016b). The forecast
 140 of concentrations is given by

$$C_i^f(t) = \psi [C_0, S_i^a(t-1)], \quad (4)$$

141 where the superscripts f and a refer to forecasted and updated values after assimilation,
 142 respectively; ψ represents the numerical model that forecast, in time, concentrations,
 143 on a grid with N_m nodes; C_i is an $N_m \times 1$ column vector containing the forecasted
 144 concentrations at all the discretization nodes of the numerical model for realization
 145 i ; S_i^a is the vector with the last updated parameters; C_0 is the initial contaminant
 146 concentration of the domain, which is the same for all realizations. The forecast of the
 147 parameters is simply

$$S_i^f(t) = S_i^a(t-1). \quad (5)$$

- 148 3. Parameters update. First compute the parameter covariance through the ensemble of
 149 forecasted realizations

$$P_S^f(t) = \frac{1}{N_e} \sum_{i=1}^{N_e} \left\{ \left[S_i^f(t) - \overline{S_i^f(t)} \right] \left[S_i^f(t) - \overline{S_i^f(t)} \right]^T \right\} \quad (6)$$

150 with

$$\overline{S_i^f(t)} = \frac{1}{N_e} \sum_{i=1}^{N_e} S_i^f(t), \quad (7)$$

151 where P_S^f is an 8×8 matrix of parameter covariances and $\overline{S_i^f(t)}$ is an 8×1 column vector
 152 of parameter averages. Then, compute the parameter-concentration cross-covariances
 153 but only with the forecasted concentration values that fall at concentration observation
 154 locations for time t (for the sake of simplicity, we will assume that observations are
 155 taken coinciding with some of the numerical model nodes, if not, there will be a need to
 156 provide a linear averaging procedure to estimate concentrations at observation locations
 157 from model concentration forecasts)

$$P_{SC}^f(t) = \frac{1}{N_e} \sum_{i=1}^{N_e} \left\{ \left[S_i^f(t) - \overline{S_i^f(t)} \right] \left[C_i^f(t) - \overline{C_i^f(t)} \right]^T \right\} \quad (8)$$

158 with

$$\overline{C_i^f(t)} = \frac{1}{N_e} \sum_{i=1}^{N_e} C_i^f(t), \quad (9)$$

159 where P_{SC}^f is an $8 \times N_o$ matrix of parameter-concentration cross-covariances, with N_o
 160 being the number of nodes of the numerical model at which observations are taken at
 161 time step t , and $\overline{C_i^f(t)}$ is an $N_o \times 1$ column vector of average concentrations. Next,
 162 compute the $8 \times N_o$ Kalman gain matrix $K(t)$ as

$$K(t) = P_S^f(t) [P_{SC}^f(t) + R(t)]^{-1} \quad (10)$$

163 where $R(t)$ is an $N_o \times N_o$ diagonal observation error covariance matrix (implying that
 164 there is no correlation between observation errors) and proceed to update the parameter
 165 values, realization by realization by

$$S_i^a(t) = S_i^f(t) + K(t) \left[d_i(t) - C_{io}^f(t) \right], \quad (11)$$

166 where $d_i(t)$ is an $N_o \times 1$ vector of observed concentrations (including observation errors
167 with covariance given by $R(t)$) and $C_{io}^f(t)$ is an $N_o \times 1$ vector of forecasted concentra-
168 tions.

169 4. Go back to step 2 and repeat the whole process until all observations are assimilated.

170 3. Experimental Case

171 3.1. Description of the experiment

172 A single point pollution experiment was performed in a sandbox using sodium fluorescein
173 as tracer. The sandbox is built in plexiglass and has external dimensions of 120 cm \times 14
174 cm \times 70 cm as sketched in Fig. 1. The internal volume of 96 cm \times 10 cm \times 70 cm is
175 filled with constant-diameter spherical glass beads. There are two reservoirs at the edges of
176 the box imposing constant water levels of 60.7 cm and 53.6 m upstream and downstream,
177 respectively. An injector was set up at the upstream part of the sandbox at the location
178 indicated by a red square in the figure, and a plastic plate was vertically inserted inside
179 the glass beads in the middle of the sandbox, whose position and length is also shown in
180 the figure. The experimental equipment was placed in a dark box and a digital camera was
181 used to capture, every 5 s, the fluorescein luminosity within the rectangular zone of 85 cm
182 by 44 cm marked with a ticked rectangle in Fig. 1. The pictures were then processed and
183 the fluorescein luminosity transformed into concentrations after a calibration procedure, as
184 described by Citarella et al. (2015). In this case, eight different fluorescein concentrations
185 ($C = 0; 2.5; 5; 10; 20; 25; 30; 35$ mg/l) were used to calibrate and generate the luminosity-
186 concentration curves in each picture pixel. The total experiment time lasted 1965 s, the
187 injection started at time 120 s and finished at time 1000 s. During the experiment, the rate
188 and concentration of the injection were also recorded.

189 It is very important to note that there are no piezometric head observations. The design
190 of the tank did not allow for those observations. Had there been piezometric head data, they

191 could have been assimilated in the filter and, without doubt, would have helped in improving
192 the identification (as shown by Xu and Gómez-Hernández (2018)).

193 *3.2. Numerical Model*

194 Since the thickness of the sandbox along the y axis is relatively small, we can assume
195 that the variability of piezometric heads and concentration along this direction is negligible.
196 Therefore, a two-dimensional groundwater flow and transport model in the XZ plane is
197 built. The upstream and downstream vertical boundaries are set as constant prescribed
198 piezometric head values, and the bottom boundary is impermeable while the top boundary
199 is the phreatic surface. The model corresponds to the yellowish area in Fig. 1, where
200 the coordinates of the four model corners are given. The tank is filled with homogeneous
201 spherical glass beads with a conductivity of 0.58 cm/s and a porosity of 0.37. The vertical
202 plastic plate was inserted at a distance of 52 cm from the left boundary and its length is of
203 42 cm. It is modeled as an impermeable barrier, which will deflect the flowlines towards the
204 bottom of the sandbox. The sandbox is discretized into 96 columns, one row, and 70 layers;
205 the size of each cell is $(\Delta x, \Delta y, \Delta z) = (1, 10, 1)$ cm. The total simulation time is 1800 s and
206 is discretized into 90 uniform time steps. Citarella et al. (2015) evaluated the longitudinal
207 and transverse dispersivities of the spherical beads, resulting in values of 0.16 cm and 0.048
208 cm, respectively. The flow and transport parameters are collected in Table 1.

209 The release happens at coordinates (18.5 cm, 30.5 cm), with a concentration of 20 mg/l
210 and an injection rate of 0.95 cm³/s. To start the ensemble Kalman filter 800 8-tuples of
211 the source and plate parameters are generated from uniform distributions (not centered at
212 the true values). The true values of the parameters to identify and the suspect range of the
213 uniform distributions used to generate the initial ensemble are collected in Table 2.

214 4. Application

215 The objective of this work is to demonstrate the capacity of the r-EnKF for the identifi-
216 cation of contaminant source information, including contaminant source location (X_s, Z_s) ,
217 injection information (I_c, I_r) and release time (T_s, T_e) together with the position and length
218 of the vertical plate (X_b, Z_b) , using concentration observations collected in a laboratory ex-
219 periment. As a prior test, we analyze a synthetic case, in which the concentration data are
220 generated by the numerical model of the sandbox, therefore removing any modeling error
221 since the forward model used to forecast by the r-EnKF will coincide with the model used to
222 generate the observations. In the next section, we will redo the analysis using the laboratory
223 data, we will analyze the problems found and propose some solutions.

224 4.1. Synthetic Sandbox Test

225 In this case, we design two scenarios $(S1, S2)$ with different number of observation wells
226 to evaluate the performance of the r-EnKF: scenario $S1$ with 20 observation wells, and
227 scenario $S2$ with 24 observation wells containing 4 additional wells ($\#21, \#22, \#23, \#24$)
228 located at the four corners of the suspect release area (see Fig. 1). The rationale for the
229 second scenario is that, after analyzing the first scenario, we felt that additional information
230 about the plume evolution was needed, and thus we decided to add four wells around the
231 suspect release zone. Such an addition will, indeed, improve the characterization. In both
232 scenarios, model error is neglected and we assume that observation errors are uncorrelated
233 with mean zero, and standard deviation of 0.1 mg/l.

234 Figure 2 and 3 show the time evolution of the ensemble mean and the ensemble variance,
235 respectively, of the updated state parameters for the two scenarios. Figure 4 shows the
236 evolution in time of the boxplots computed from the 800 ensemble members. After time
237 step 60, the convergence rate of the means and variances of the parameters are less than 1%
238 and 5%, respectively, all the parameters get close to the final estimation and become stable.
239 Notice also the sudden drop of the variance at a given time step for most of the parameters.

240 This drop is related to the activation of new observation wells as time progresses, what
241 implies that the amount of information assimilated by the filter does not vary continuously
242 in time, but rather it increases stepwise, with steps occurring when new wells observe, for
243 the first time, the arrival of the solute plume. We can distinguish between the parameters
244 that are perfectly identified by an ensemble mean equal to the true value, and practically
245 zero variance, and those that are approximated closely but which are not exact and present
246 some residual uncertainty. In the first group, there are the position parameters for the plate,
247 Xb and Zb , plus the vertical location of the release source Zs , independently of whether 20
248 or 24 data are used during the assimilation steps; in the second group are the remaining
249 parameters, which become more precise (mean closer to the true value) and less uncertain
250 (smaller variability) for $S2$ than for $S1$. The horizontal source location Xs is less sensitive
251 to the concentration data, and only when the four additional data points in the corners of
252 the suspect release location are added the algorithm is able to provide a good estimate for
253 this parameter; similar comment can be made about the beginning Ts and end Te times
254 of the release. The injection concentration Ic and injection rate Ir are well identified by
255 their median values, with smallest uncertainty for $S2$. These results are consistent with
256 the sensitivity of concentrations at the observation locations to changes in the parameter
257 values: concentration distributions are most sensitive to the position of the plate, which
258 affects the flow field, and the vertical release location, which affects the main trajectory of
259 the contaminant plume, but are less sensitive to the other parameters, for which variations
260 within the identified uncertainty ranges induce concentration changes of the same order of
261 magnitude as the observation errors. Also notice that the horizontal coordinate of the release
262 and the starting and ending release times are correlated for the purpose of identifying their
263 values (a displacement of the horizontal coordinate of the release could be compensated with
264 a displacement of its starting time), what also explains their larger uncertainties.

265 These results prove that the r-EnKF could work for the identification of a contaminant
266 source and of some parameters defining the geometry of the aquifer. The next step is to test

267 the algorithm under more realistic conditions using observations obtained from a laboratory
268 experiment.

269 4.2. Laboratory Sandbox Test

270 The sandbox experiment was carried out as described previously. Figure 5 shows a
271 picture of the fluorescein plume at the 48th time step (840 s since the beginning of the
272 release) already transformed into concentration values and the position of the observation
273 points. The deflection of the flowlines induced by the vertical plate is clearly seen. Notice
274 that only a few observation piezometers will actually detect the plume breakthrough. Before
275 testing the r-EnKF, we performed a simulation of the concentration evolution using the
276 known release parameters and compared the predictions with the observed data. Figure
277 6 shows a comparison between observed and numerically predicted concentrations at five
278 observation locations (wells #7, #9, #10, #13, #22) through which the plume passes. As
279 can be seen, the reproduction is very good for the closest well #22, and it deteriorates with
280 the distance from the source, but not dramatically, except for well #9. For this well, the
281 beginning and ending times of the breakthrough curve are the same for predictions and
282 observations, but the mismatch in concentrations indicates either some error in the model
283 parameters or faulty observations. The predicted breakthrough curve in the farthest well,
284 though, is quite close to the observed one. In the application that follows we will analyze
285 different observation error distributions in an attempt to identify the source parameters by
286 the r-EnKF.

287 We have run the r-EnKF with three different magnitudes of the observation error, which
288 will be referred to as $R1$, $R2$, and $R3$. In all three cases, the error mean is zero and its
289 standard deviation is 0.5 mg/l for $R1$, 1.0 mg/l for $R2$, and 3.0 mg/l for $R3$. We must
290 notice that in previous experiments, Cupola et al. (2015a) report an observation error with
291 a standard deviation around 1 mg/l.

292 The hydraulic conductivity value of the beads, which is considered homogeneous in each

293 realization, is considered uncertain and drawn from a Gaussian distribution with a mean
294 of 0.58 cm/s and a standard deviation of 0.05 cm/s. We have decided to introduce some
295 uncertainty on the beads hydraulic conductivity as a surrogate to model error. The choice of
296 a Gaussian distribution centered at the calibrated conductivity value was arbitrary, any other
297 distribution could have been used. Considering that the differences in the results between
298 including or not such an uncertainty are minimal (and not reported here), we believe that
299 the choice of the specific distribution has little effect in the final outcome.

300 Fig. 7 shows the boxplots of the updated parameters at different time steps for the three
301 scenarios *R1*, *R2*, and *R3*. The results are not as good as for the synthetic case, for which the
302 observed concentrations were generated with the same numerical model used for the forecast
303 step in the Kalman filter. The first thing to note is that for scenario *R1*, the use of a small
304 observation error makes the r-EnKF to seek for source parameter values that can be far
305 from the true ones in order to produce concentrations that are close to the observed values,
306 and, particularly, the injection concentration and injection rate do not seem to converge to
307 a stable value after 90 time steps. The other parameters do reach a stable median, not as
308 close to the true values as for the synthetic case but close enough except for the horizontal
309 position of the vertical plate.

310 When the observation error is increased (scenario *R2*), the two main findings are that the
311 two injection parameters now seem to reach a stable estimate (albeit with large uncertainty)
312 with a median close to the true value, and that all parameters have a wider uncertainty range.
313 The median estimate of the initial and ending release times is also closer to the true ones
314 than in *R1*. The horizontal position of the vertical plate continues to be underestimated, as
315 well as the length of the plate.

316 When the observation error is increased even more (scenario *R3*) the main effect is that
317 the final estimates have wide uncertainty estimates, and for some of the parameters it seems
318 as if the concentration observations do not bring any added value since the boxplot width
319 remains unaltered through the assimilation steps. The estimates of the parameters by their

320 median is comparable to the results in *R2*, but their uncertainty is larger.

321 The predicted concentrations at three observation wells that were not used during the
322 assimilation step computed using the initial 8-tuples of parameters, and using the 8-tuples
323 obtained at the end of the three scenarios are shown in Figure 8. The figure shows the
324 true concentrations in the sandbox as a dotted blue line, each one of the 800 predicted
325 concentration breakthrough curves computed with the 8-tuples of the ensemble, along with
326 their median, as a red line, and their 90% confidence interval, as dashed lines. It can be
327 observed that, prior to assimilation (top row), concentration predictions were very scattered,
328 and that after the assimilation (bottom three rows, one for each scenario) the breakthrough
329 curves change substantially (compare, for instance, the median curves). For scenario *R1*, the
330 scatter of prediction curves is the smallest but recall that these wells were not used during
331 the assimilation, the updated parameters were biased because the algorithm tried to fit the
332 observed concentrations too closely and as a result, at the control wells, the prediction of
333 the true curves by the ensemble median is also biased, up to the point that the true curves
334 are outside the 90% confidence interval. For scenarios *R2* and *R3* the median curves for the
335 three wells have a smaller bias than for *R1*, and the main difference between *R2* and *R3* is
336 the same as for parameter prediction, the uncertainty is the widest for *R3*. The true curve
337 is in both cases within the 90% confidence interval of the predictions.

338 At this point, it seems that an observation error with a standard deviation of 1 mg/l was
339 the most consistent with our observations and model. As mentioned above, this conclusion
340 fits the findings by Cupola et al. (2015a). Yet, we were concerned with the big discrepancy
341 between predictions and observations at well #9, so we decided to rerun scenario *R2* without
342 using the data from this well. The results for this scenario, called *R2b*, are shown in Figure
343 9. When comparing this figure to the middle two rows in Figure 7 we can notice that there
344 is some overall improvement in the estimation of the true parameters —particularly for the
345 position parameters— by the median values of the ensemble without a significant change
346 on their uncertainty. This improvement reinforces our suspicion that there could have been

347 some problems in the data collection at well #9.

348 We also considered that there could be a problem with the tightness of the vertical
349 plate after its insertion in the sandbox. The plate was supposed to represent a perfectly
350 impermeable barrier, and no evidence of the contrary was observed during the experiments,
351 yet the contact between the plate and sandbox walls could have had some small gaps, making
352 the plate slightly permeable. Therefore, we decided to rerun scenario *R2* but assuming that
353 the plate is slightly permeable, more precisely, with a conductivity of two orders of magnitude
354 smaller than the beads, this value was chosen arbitrarily low since nothing was actually
355 observed in the laboratory. The results for the new scenario, referred to as *R2c* are shown in
356 Figure 10. (Note that well #9 was kept in this scenario.) The main difference of this run is
357 that the estimate of the size of the vertical plate by the median of the ensemble jumps from
358 40.5 cm to 44.2 cm (true value is 42.0 cm) indicating that possibly the plate conductivity
359 used in this scenario was too large and, as a consequence, the algorithm enlarges the plate
360 to reproduce the observed concentrations. This result, while does not serve to justify that
361 the tightness of the plate explains the numerical model misfit, shows the impact that such
362 permeability would have in the estimation of the remaining parameters defining the plate.

363 We can conclude that the r-EnKF can be applied to a more realistic case of a homogeneous
364 aquifer in a sandbox for the identification of a contaminant source and some geometry
365 parameters. A proper evaluation of the observation errors is paramount, since attempting
366 to match too closely the data may result in biased estimates of the parameters.

367 5. Summary and Conclusion

368 The main purpose of this paper was to test whether the restart ensemble Kalman filter,
369 which had been successfully applied in synthetic experiments, could be applied to a more
370 realistic case based on a sandbox experiment. The test focuses on the identification of the
371 parameters defining a finite-pulse point injection of a solute, together with the position of a
372 vertical plate that modifies the initial rectangular geometry of the sandbox.

373 As a preliminary step, we tested the r-EnKF in a synthetic case mimicking the sandbox.
374 Under these very controlled conditions, the algorithm performs well, as expected. The main
375 difference with previous synthetic analyses is that no piezometric head data were used during
376 the assimilation step of the filter.

377 Then, the r-EnKF is tested using the data coming from the laboratory experiment. In this
378 case, the observations were not generated by a computer code nor we knew the observation
379 error magnitude. The analysis of the results show that using a too small observation error
380 variance results in more or less precise but biased estimates, both for the parameters subject
381 to identification and for the concentrations at control locations. When a larger observation
382 error (with a standard deviation of 1 mg/l) is introduced, estimates and predictions improve,
383 although with larger uncertainty. And finally, when the observation error is large, the results
384 worsen considerably. The removal of a suspicious observation well, the concentration of which
385 is always underestimated by our forecast model, improves the results, indicating that the
386 measurements from such well may need to be reconsidered. The changes observed after
387 making the vertical plate slightly permeable do not appear to justify the hypothesis that the
388 plate leaks.

389 The r-EnKF appears as a good algorithm for source identification in aquifers, yet it still
390 needs further tests in closer-to-reality conditions. Currently, the sandbox has been replaced
391 with a heterogeneous distribution of glass beads, and the challenge is to test the method in
392 this new sandbox.

393 **Acknowledgements** Financial support to carry out this work was received from the
394 Spanish Ministry of Economy and Competitiveness through project CGL2014-59841-P, and
395 from the Spanish Ministry of Education, Culture and Sports through a fellowship for the
396 mobility of professors in foreign research and higher education institutions to the second
397 author, reference PRX17/00150. The authors also would like to thank Università degli
398 Studi di Parma for providing the experimental equipment and data.

399 **References**

- 400 Atmadja, J., Bagtzoglou, A.C., 2001. State of the Art Report on Mathematical Methods for
401 Groundwater Pollution Source Identification. *Environmental Forensics* 2, 205–214.
- 402 Ayvaz, M.T., 2010. A linked simulation-optimization model for solving the unknown ground-
403 water pollution source identification problems. *Journal of Contaminant Hydrology* 117,
404 46–59.
- 405 Bagtzoglou, A.C., Atmadja, J., 2005. Mathematical Methods for Hydrologic Inversion: The
406 Case of Pollution Source Identification. *Water Pollution* 5, 65–96.
- 407 Bagtzoglou, A.C., Dougherty, D.E., Tompson, A.F.B., 1992. Application of particle methods
408 to reliable identification of groundwater pollution sources. *Water Resources Management*
409 6, 15–23.
- 410 Butera, I., Tanda, M.G., Zanini, A., 2013. Simultaneous identification of the pollutant release
411 history and the source location in groundwater by means of a geostatistical approach.
412 *Stochastic Environmental Research and Risk Assessment* 27, 1269–1280.
- 413 Chen, Y., Zhang, D., 2006. Data assimilation for transient flow in geologic formations via
414 ensemble Kalman filter. *Advances in Water Resources* 29, 1107–1122.
- 415 Citarella, D., Cupola, F., Tanda, M.G., Zanini, A., 2015. Evaluation of dispersivity coeffi-
416 cients by means of a laboratory image analysis. *Journal of Contaminant Hydrology* 172,
417 10–23.
- 418 Cupola, F., Tanda, M.G., Zanini, A., 2015a. Contaminant release history identification in
419 2-d heterogeneous aquifers through a minimum relative entropy approach. *SpringerPlus*
420 4, 656.

- 421 Cupola, F., Tanda, M.G., Zanini, A., 2015b. Laboratory sandbox validation of pollutant
422 source location methods. *Stochastic Environmental Research and Risk Assessment* 29,
423 169–182.
- 424 Evensen, G., 2003. The Ensemble Kalman Filter: Theoretical formulation and practical
425 implementation. *Ocean Dynamics* 53, 343–367.
- 426 Gorelick, S.M., Evans, B., Remson, I., 1983. Identifying sources of groundwater pollution:
427 An optimization approach. *Water Resources Research* 19, 779–790.
- 428 Houtekamer, P.L., Mitchell, H.L., 2001. A Sequential Ensemble Kalman Filter for Atmo-
429 spheric Data Assimilation. 0203058.
- 430 Koch, J., Nowak, W., 2016. Identification of contaminant source architectures - A statisti-
431 cal inversion that emulates multiphase physics in a computationally practicable manner.
432 *Water Resources Research* 52, 1009–1025. 2014WR016527.
- 433 Li, L., Zhou, H., Gómez-Hernández, J.J., Hendricks Franssen, H.J., 2012a. Jointly map-
434 ping hydraulic conductivity and porosity by assimilating concentration data via ensemble
435 Kalman filter. *Journal of Hydrology* 428-429, 152–169.
- 436 Li, L., Zhou, H., Hendricks Franssen, H.J., Gómez-Hernández, J.J., 2012b. Groundwater flow
437 inverse modeling in non-MultiGaussian media: Performance assessment of the normal-
438 score Ensemble Kalman Filter. *Hydrology and Earth System Sciences* 16, 573–590.
- 439 Liu, C., Ball, W.P., 1999. Application of inverse methods to contaminant source identification
440 from aquitard diffusion profiles at dover afb, delaware. *Water Resources Research* 35,
441 1975–1985.
- 442 Mahar, P.S., Datta, B., 2000. Identification of Pollution Sources in Transient Groundwater
443 Systems. *Water Resources Management* 14, 209–227.

444 McDonald, J.M., Harbaugh, A.W., 1988. A modular three-dimensional finite-difference flow
445 model. *Techniques of Water Resources Investigations of the U.S. Geological Survey, Book*
446 *6*, 586.

447 Michalak, A.M., 2003. A method for enforcing parameter nonnegativity in Bayesian in-
448 verse problems with an application to contaminant source identification. *Water Resources*
449 *Research* 39, 1–14.

450 Michalak, A.M., Kitanidis, P.K., 2004. Estimation of historical groundwater contaminant
451 distribution using the adjoint state method applied to geostatistical inverse modeling.
452 *Water Resources Research* 40.

453 Neupauer, R.M., Wilson, J.L., 1999. Adjoint method for obtaining backward-in-time location
454 and travel time probabilities of a conservative groundwater contaminant. *Water Resources*
455 *Research* 35, 3389–3398.

456 Sun, A.Y., Painter, S.L., Wittmeyer, G.W., 2006. A constrained robust least squares ap-
457 proach for contaminant release history identification. *Water Resources Research* 42, 1–13.

458 Wagner, B.J., 1992. Simultaneous parameter estimation and contaminant source character-
459 ization for coupled groundwater flow and contaminant transport modelling. *Journal of*
460 *Hydrology* 135, 275–303.

461 Woodbury, A., Sudicky, E., Ulrych, T.J., Ludwig, R., 1998. Three-dimensional plume source
462 reconstruction using minimum relative entropy inversion. *Journal of Contaminant Hydrol-*
463 *ogy* 32, 131–158.

464 Woodbury, A.D., Ulrych, T.J., 1996. Minimum relative entropy inversion: Theory and ap-
465 plication to recovering the release history of a groundwater contaminant. *Water Resources*
466 *Research* 32, 2671–2681.

- 467 Xu, T., Gómez-Hernández, J.J., 2015. Inverse sequential simulation: A new approach for the
468 characterization of hydraulic conductivities demonstrated on a non-Gaussian field. *Water*
469 *Resources Research* 51, 2227–2242. 2014WR016527.
- 470 Xu, T., Gómez-Hernández, J.J., 2016a. Characterization of non-Gaussian conductivities and
471 porosities with hydraulic heads, solute concentrations, and water temperatures. *Water*
472 *Resources Research* 52, 6111–6136.
- 473 Xu, T., Gómez-Hernández, J.J., 2016b. Joint identification of contaminant source location,
474 initial release time, and initial solute concentration in an aquifer via ensemble Kalman
475 filtering. *Water Resources Research* .
- 476 Xu, T., Gómez-Hernández, J.J., 2018. Simultaneous identification of a contaminant source
477 and hydraulic conductivity via the restart normal-score ensemble Kalman filter. *Advances*
478 *in Water Resources* 112, 106–123.
- 479 Xu, T., Gómez-Hernández, J.J., Zhou, H., Li, L., 2013a. The power of transient piezometric
480 head data in inverse modeling: An application of the localized normal-score EnKF with
481 covariance inflation in a heterogenous bimodal hydraulic conductivity field. *Advances in*
482 *Water Resources* 54, 100–118.
- 483 Xu, T., Jaime Gómez-Hernández, J., Li, L., Zhou, H., 2013b. Parallelized ensemble Kalman
484 filter for hydraulic conductivity characterization. *Computers and Geosciences* 52, 42–49.
- 485 Yeh, H.D., Chang, T.H., Lin, Y.C., 2007. Groundwater contaminant source identification
486 by a hybrid heuristic approach. *Water Resources Research* 43, 1–16.
- 487 Zanini, A., Woodbury, A.D., 2016. Contaminant source reconstruction by empirical Bayes
488 and Akaike’s Bayesian Information Criterion. *Journal of Contaminant Hydrology* 185-186,
489 74–86.

- 490 Zheng, C., Wang, P.P., 1999. MT3DMS: A Modular Three-Dimensional Multispecies Trans-
491 port Model , 219.
- 492 Zhou, H., Gómez-Hernández, J.J., Hendricks Franssen, H.J., Li, L., 2011. An approach to
493 handling non-Gaussianity of parameters and state variables in ensemble Kalman filtering.
494 Advances in Water Resources 34, 844–864.
- 495 Zhou, H., Gómez-Hernández, J.J., Li, L., 2014. Inverse methods in hydrogeology: Evolution
496 and recent trends. Advances in Water Resources 63, 22–37.

Table 1: Parameters of the groundwater flow and transport model

Hydr. conduct., K	0.58 cm/s
Porosity, ϕ	0.37
Long. disp., α_L	0.16 cm
Transv. disp., α_T	0.048 cm

Table 2: Source and geometry parameters. True values and suspect ranges for the generation of the initial ensemble of realizations

Parameter	Actual Value	Suspect Range
X_s (cm) - x -coordinate of source	18.5	16 – 25
Z_s (cm) - z -coordinate of source	30.5	23 – 32
X_b (cm) - x -coordinate of plate	52.5	50 – 59
Z_b (cm) - plate length	42.5	35 – 43
I_r (cm ³ /s) - injection rate	0.95	0.6 – 1.1
I_c (mg/l) - injection load	20	5 – 24
T_s (s) - starting release time	120	80 – 260
T_e (s) - ending release time	1000	960 – 1140

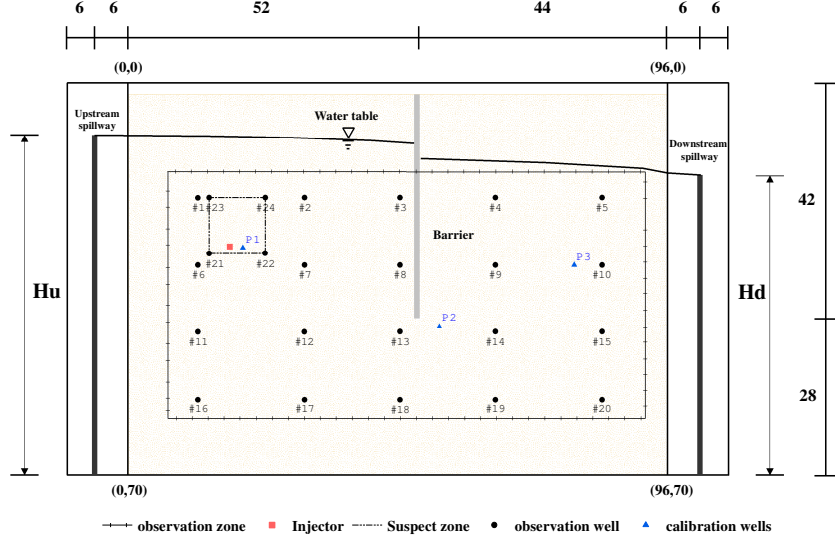


Figure 1: Sketch of the experimental device with indication of the upstream (H_u) and downstream (H_d) constant head boundaries. The ticked rectangle corresponds to the area captured by the camera in which concentrations will be monitored. Red dot is the release location. Dashed line around red dot indicates the release suspect location. Dimensions are in cm. Coordinates of the four corners of the flow and transport models are also shown.

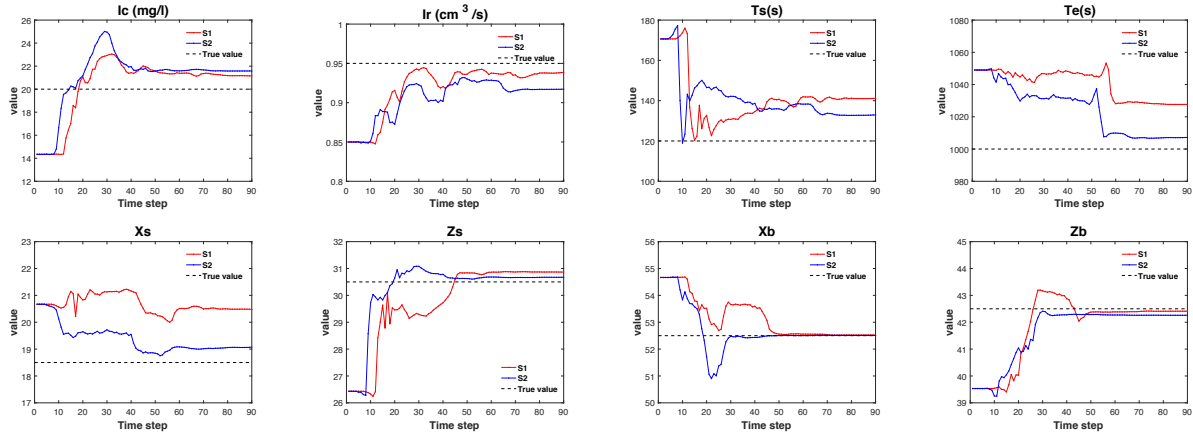


Figure 2: Time evolution of the ensemble mean of the 8 updated parameters, contaminant source location (X_s , Z_s), plate position (X_b , Z_b), injection information (I_c , I_r) and release time interval (T_s , T_e) for scenarios S_1 and S_2

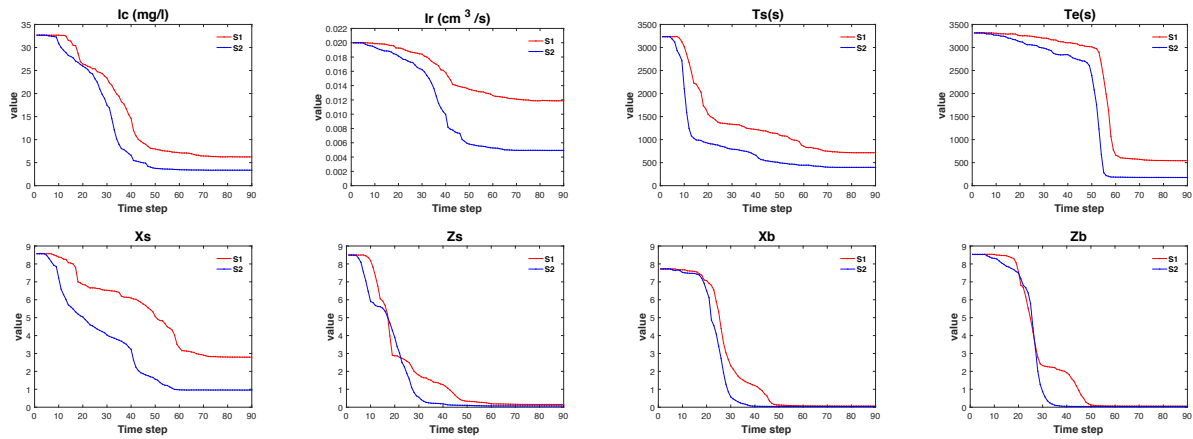


Figure 3: Time evolution of the ensemble variance for the same parameters and scenarios as in the previous figure.

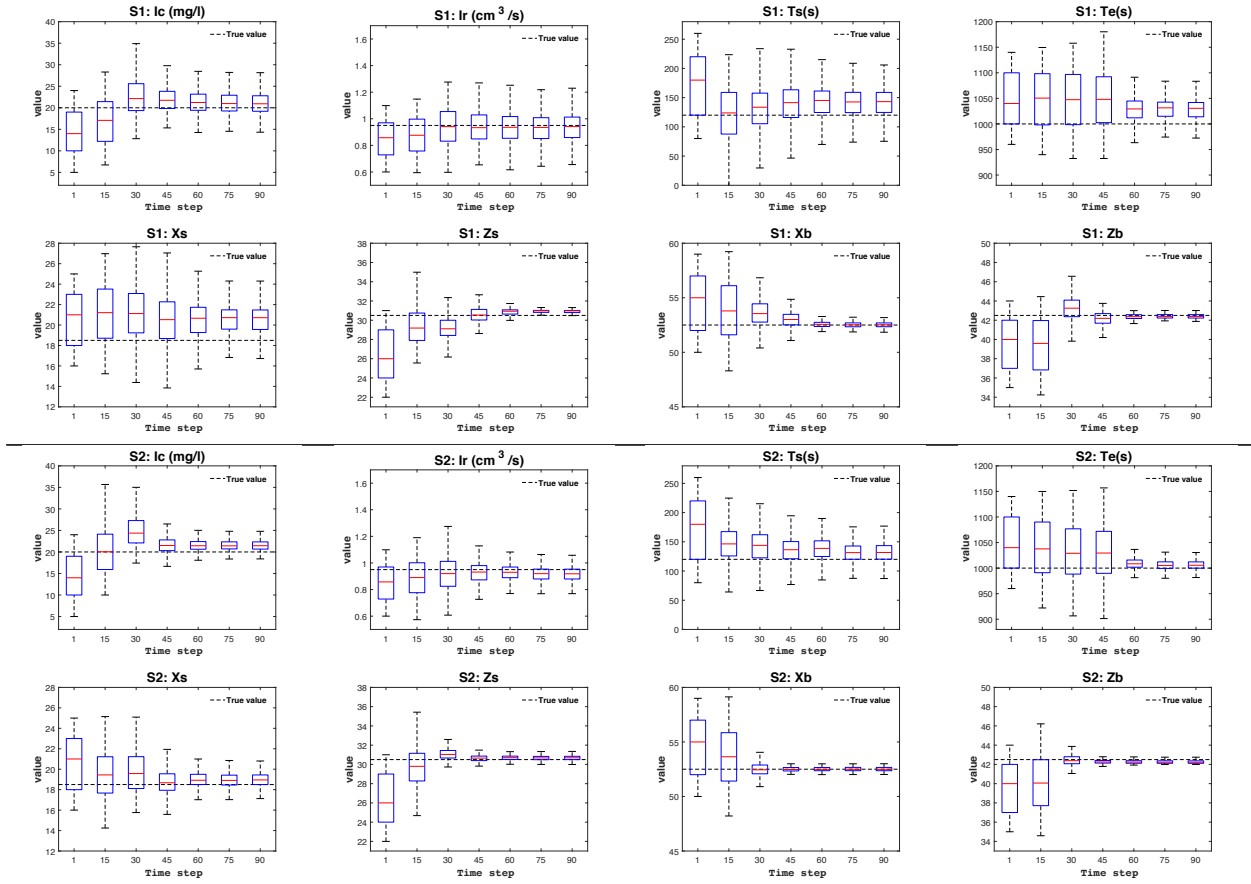


Figure 4: Boxplot of the 8 updated parameters at different time steps (1, 15, 30, 45, 60, 75, 90) for scenarios S1 and S2

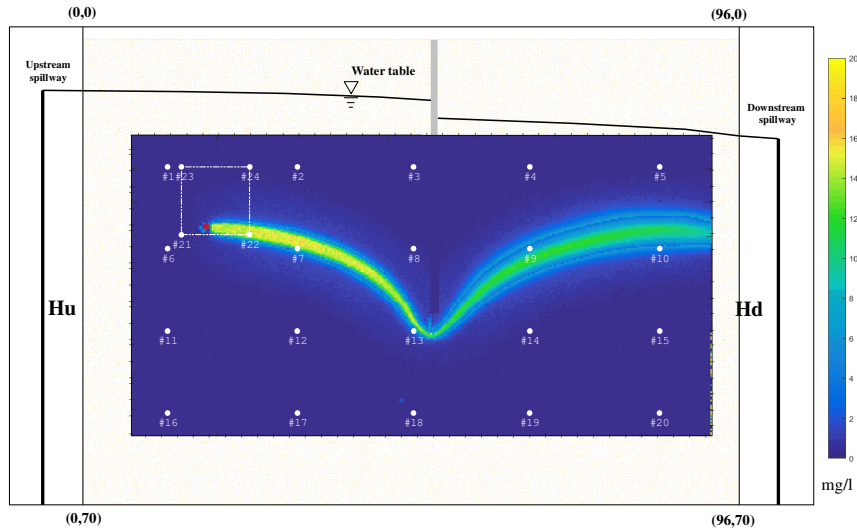


Figure 5: Fluorescein concentration field in the sandbox at the 48th time step. The area shown corresponds to the observation zone indicated in Fig. 1. The dash line shows the suspect zone for the injection and the white dots indicate the observation wells.

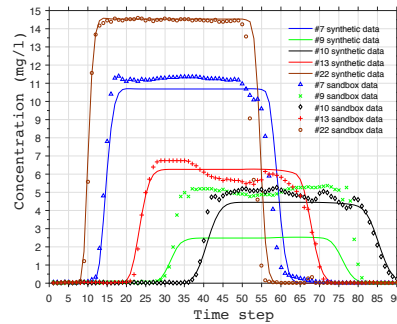


Figure 6: Fluorescein observed breakthrough curves at the observation wells located inside the plume and the curves computed from the numerical model

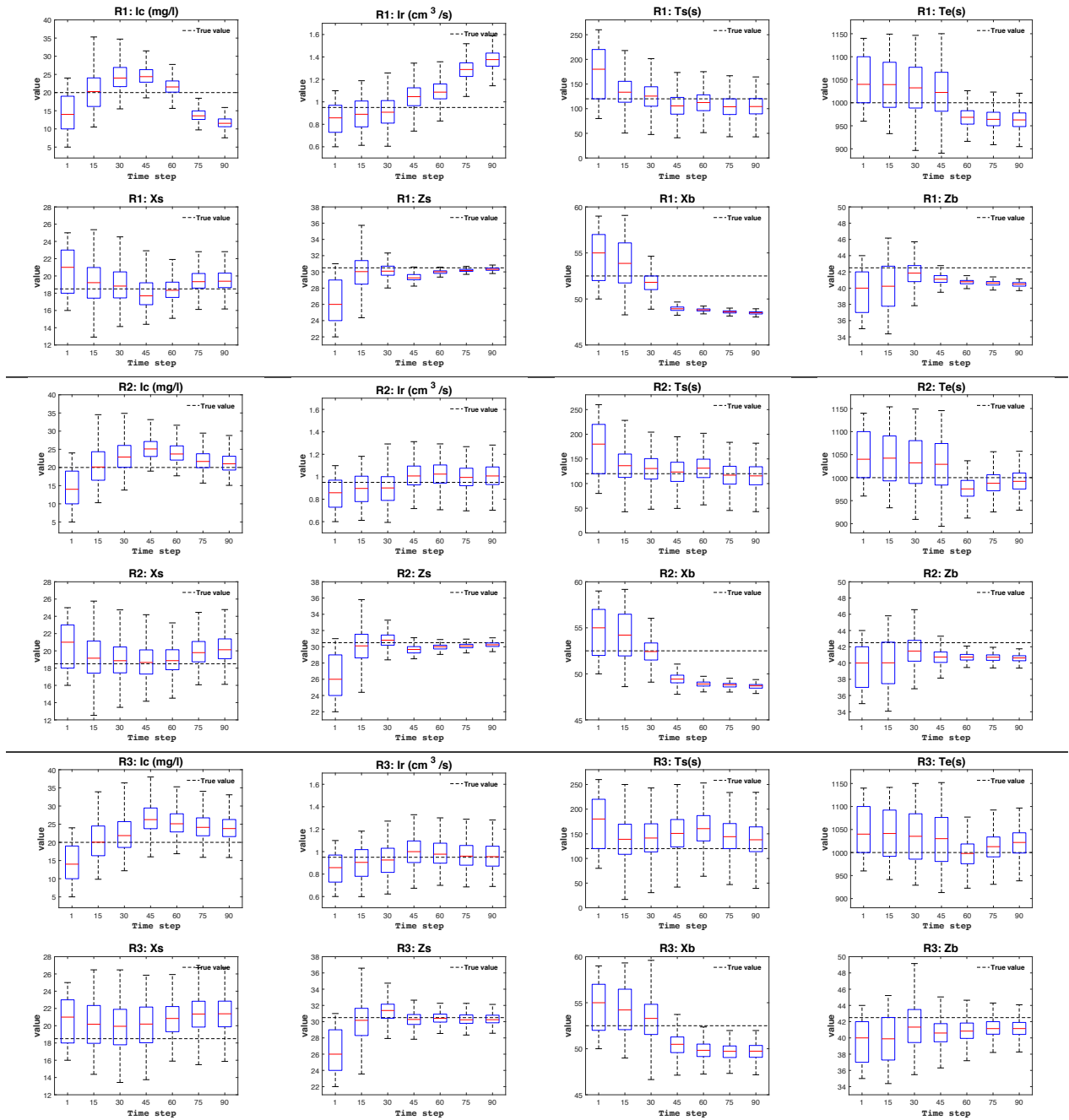


Figure 7: Boxplot of of the 8 updated parameters at time steps 1, 15, 30, 45, 60, 75 and 90 for scenarios $R1$, $R2$ and $R3$

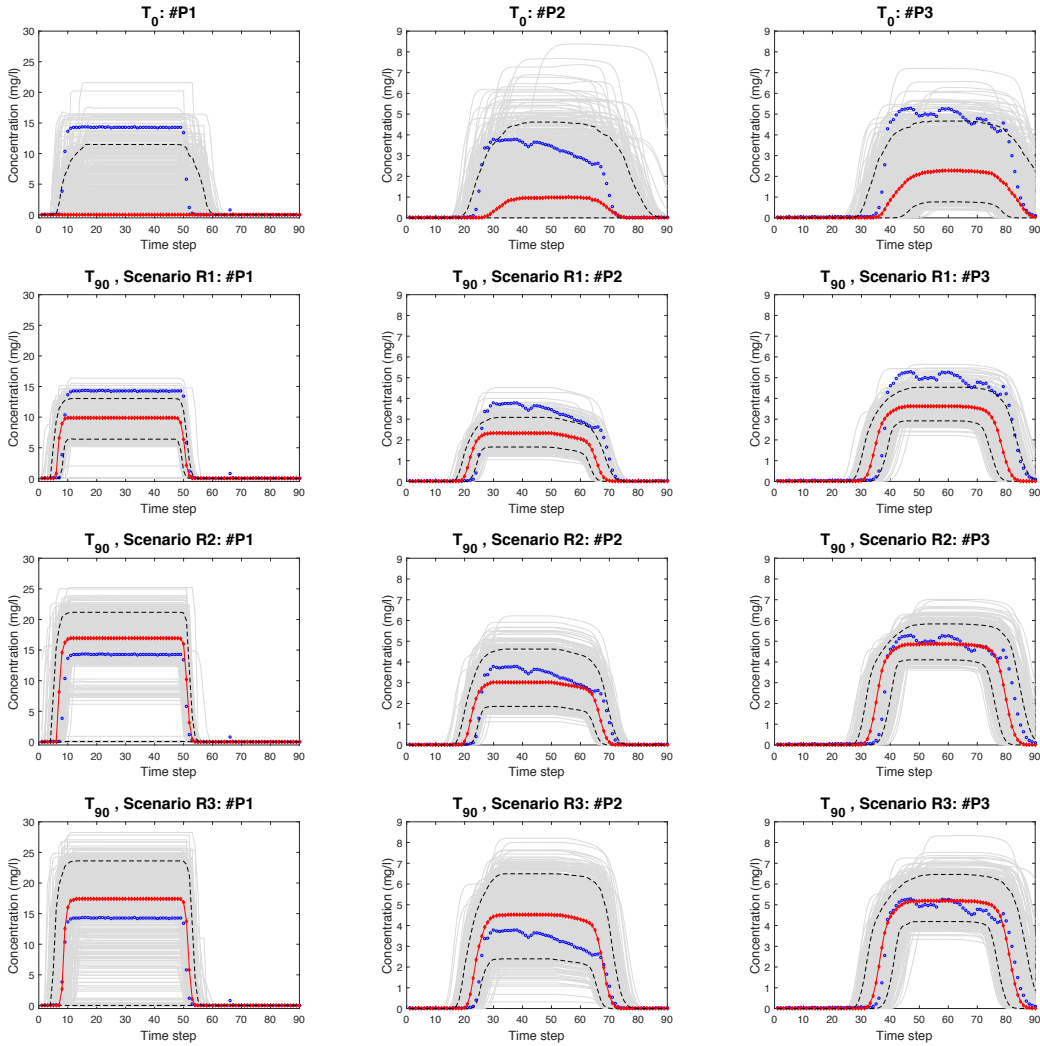


Figure 8: Breakthrough curves at control wells. The blue dots correspond to the curves in the sandbox experiment. The thin gray lines are the curves for all 800 realizations; they are summarized by their median (red diamond lines) and their 5 and 95 percentiles (black dash lines).

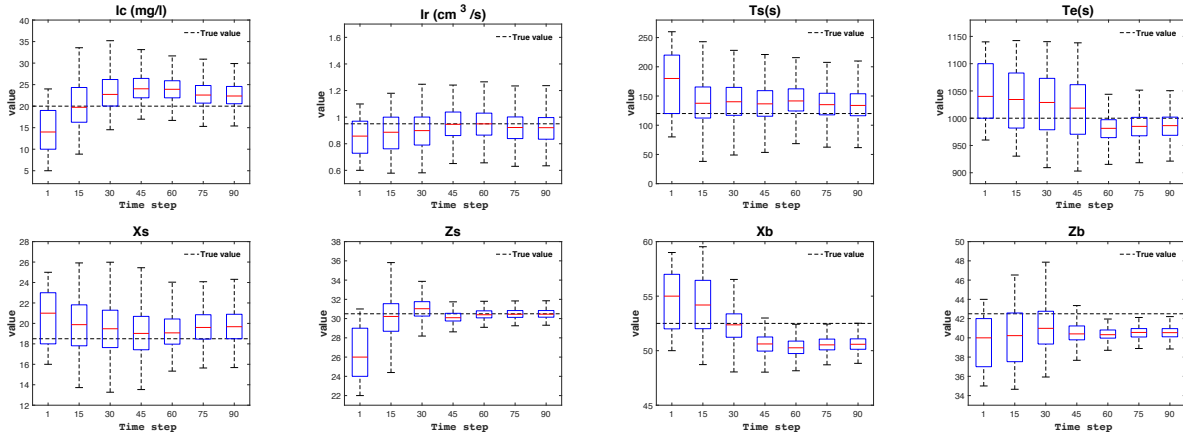


Figure 9: Boxplot of the 8 updated parameters in scenario *R2b* at different time steps (1, 15, 30, 45, 60, 75, 90)

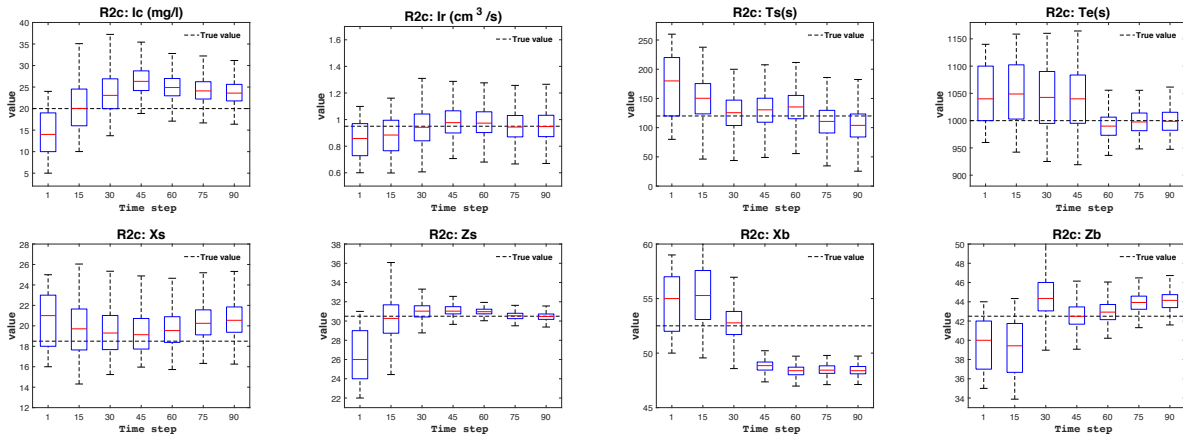


Figure 10: Boxplot of the 8 updated parameters in scenario *R2c* at different time steps (1, 15, 30, 45, 60, 75, 90)

Joint identification of contaminant source and aquifer geometry in a sandbox experiment with the restart Ensemble Kalman filter

Zi Chen^a, J. Jaime Gómez-Hernández^a, Teng Xu^{a,*}, Andrea Zanini^b

^a*Institute of Water and Environmental Engineering, Universitat Politècnica de València, Valencia, Spain*

^b*Dipartimento di Ingegneria e Architettura, Università degli Studi di Parma, Parma, Italy*

Abstract

Contaminant source identification is a key problem in handling groundwater pollution events. The ensemble Kalman filter (EnKF) is used for the spatiotemporal identification of a point contaminant source in a sandbox experiment, together with the identification of the position and length of a vertical plate inserted in the sandbox that modifies the geometry of the system. For the identification of the different parameters, observations in time of solute concentration are used, but not of piezometric head data since they were not available. A restart version of the EnKF is utilized because it is necessary to restart the forecast from time zero after each parameter update. The results show that the restart EnKF is capable of identifying both contaminant source information and aquifer-geometry-related parameters together with an uncertainty estimate of such identification.

Keywords: Inverse modeling; Observation error; Groundwater laboratory experiment; Stochastic hydrogeology

1. Introduction

2 The problem of identifying a contaminant source in an aquifer using solute concentra-
3 tion data has been the subject of attention for many years (e.g., Atmadja and Bagtzoglou,

*Corresponding author

Email address: tenxu@posgrado.upv.es (Teng Xu)

4 2001; Michalak and Kitanidis, 2004; Bagtzoglou and Atmadja, 2005; Sun et al., 2006, and
5 references therein). Briefly, the proposed methods could be grouped into two categories:
6 optimization approaches and probabilistic approaches. The main difference between the two
7 approaches is that the optimization approaches cast the problem as a deterministic one in
8 which parameters are found that minimize a given objective function, whereas the probabilis-
9 tic approaches cast the problem in a stochastic framework and the parameters to estimate
10 become random variables. In the first category, Gorelick et al. (1983) identified the ground-
11 water pollution source information through an optimization model using linear programming
12 and multiple regression; Wagner (1992) employed a non-linear maximum likelihood method
13 to estimate source location and flux; Mahar and Datta (2000) used a nonlinear optimization
14 model for estimating the magnitude, location and duration of groundwater pollution sources
15 with binding equality constraints; Yeh et al. (2007) developed a hybrid approach, which
16 combines simulated annealing, tabu search and a three-dimensional groundwater flow and
17 solute transport model to solve the source identification problem; and Ayvaz (2010) utilized
18 a harmony search-based simulation-optimization model to determine the source location and
19 release histories by using an implicit solution procedure. In the second category, Bagtzoglou
20 et al. (1992) applied a particle method to estimate, probabilistically, source location and
21 spill-time history; Woodbury and Ulrych (1996) used a minimum relative entropy approach
22 to recover the release and evolution histories of a groundwater contaminant plume in a one-
23 dimensional system; Neupauer and Wilson (1999) employed a backward location model based
24 on adjoint state method (BPM-ASM) to identify a contaminant source; Butera et al. (2013)
25 utilized a simultaneous release function and source location identification (SRSI) method to
26 identify the release history and source location of an injection in a groundwater aquifer; and
27 Koch and Nowak (2016) derived and applied a Bayesian reverse-inverse methodology to infer
28 source zone architectures and aquifer parameters.

29 The ensemble Kalman filter (EnKF), which could be included in the group of probabilistic
30 approaches mentioned above, has recently addressed the problem of contaminant source

31 identification. The EnKF introduced by Evensen (2003) has gained much popularity in recent
32 years for its efficiency in solving inverse problems in different fields such as oceanography,
33 meteorology and hydrology (Houtekamer and Mitchell, 2001; Li et al., 2012a; Xu et al.,
34 2013b). The advantages of the EnKF can be summarized as follows (Chen and Zhang, 2006;
35 Zhou et al., 2011): computational efficiency when compared with other inverse approaches,
36 easy integration with different forecast models, ability to account for model and observation
37 errors, and easy uncertainty characterization since the final outcome is always an ensemble
38 of realizations. In hydrogeology, the EnKF has been mainly applied for the identification of
39 aquifer parameters such as hydraulic conductivity or porosity (Li et al., 2012b; Xu et al.,
40 2013a; Zhou et al., 2014; Xu and Gómez-Hernández, 2015, 2016a). Recently, Xu and Gómez-
41 Hernández (2016b) demonstrated the possibility to apply the EnKF for the identification of a
42 contaminant source in a deterministic synthetic aquifer, and later Xu and Gómez-Hernández
43 (2018) showed that the method can be also applied for the simultaneous identification of
44 hydraulic conductivities and the parameters defining a contaminant source also in a synthetic
45 aquifer.

46 All the works mentioned above were tested in synthetic cases. Only a few works can be
47 found in the literature for laboratory or field cases. Woodbury et al. (1998) extended the
48 minimum relative entropy (MRE) method to recover the release history of a contaminant and
49 applied it to reconstruct the release history of a 1,4-dioxane plume observed at the Gloucester
50 Landfill in Ontario, Canada. Michalak (2003); Michalak and Kitanidis (2004) employed a
51 Bayesian inverse formulation to estimate the contaminant history of trichloroethylene (TCE)
52 and perchloroethylene (PCE) in an aquifer at the Dover Air Force Base, Delaware, a site that
53 had already been analyzed by Liu and Ball (1999) in the same context of source identifica-
54 tion. Cupola et al. (2015b,a) compared the source location identification (SRSI) method to
55 the backward probability model based on the adjoint state method (BPM-ASM) with data
56 taken from a sandbox experiment. Zanini and Woodbury (2016) also used data from a sand-
57 box experiment to apply an empirical Bayesian method combined with Akaike's Bayesian

58 Information Criterion (ABIC) to deduce the release history of a groundwater contaminant.

59 The main objective of this paper is to assess the performance of the restart EnKF (r-
60 EnKF) for the identification of contaminant source parameters and aquifer geometry with
61 data from a sandbox experiment. The source parameters of interest are the release location,
62 release starting and ending times, and contaminant load, and regarding the geometry the
63 method should try to retrieve the position and length of a plate that is inserted about the
64 center of the sandbox and induces a deflection of the flowlines towards the bottom of the
65 sandbox. The state information assimilated by the r-EnKF is limited to concentration data
66 at a few observation points, since no piezometric head data were available.

67 The paper is organized as follows, first, the state equations and the fundamentals of the
68 r-EnKF will be recalled, second, the sandbox characteristics are described together with the
69 numerical model used to reproduce its behavior, third, the r-EnKF is tested with data from
70 a synthetic experiment that mimics the sandbox experiment with the aim to verify if the r-
71 EnKF is capable of identifying the kind of parameters sought, and four, the r-EnKF is applied
72 with observation values taken from the sandbox experiment, the problems encountered are
73 analyzed, alternative approaches are discussed and the final results presented. The paper
74 ends with a summary and conclusions on the main findings.

75 **2. Methodology**

76 *2.1. Groundwater Flow and Solute Transport Equation*

77 The sandbox will be modeled as a two-dimensional system in the XZ plane, where an
78 inert contaminant spreads due to advection and dispersion under a steady-state flow. The
79 dimension of the sandbox in the y direction is small enough to assume that the state variables
80 are constant along any line for any given (x, z) value. The governing equations are:

$$\frac{\partial}{\partial x} \left(K_x \frac{\partial h}{\partial x} \right) + \frac{\partial}{\partial z} \left(K_z \frac{\partial h}{\partial z} \right) + w = 0 \quad (1)$$

$$\frac{\partial(\theta C)}{\partial t} = \nabla \cdot (\theta D \cdot \nabla C) - \nabla \cdot (\theta v C) - q_s C_s \quad (2)$$

81 where K_x and K_z are the principal components of the hydraulic conductivity tensor in the x
 82 and z spatial coordinates respectively [LT^{-1}] which are assumed aligned with the coordinate
 83 system of reference in the entire domain; h is the hydraulic head [L]; w represents distributed
 84 sources or sinks [T^{-1}]; t is time [T]; θ represents the porosity of the medium; C is dissolved
 85 concentration [ML^{-3}]; $\nabla \cdot$ is the divergence operator; ∇ is the gradient operator; D represents
 86 the hydrodynamic dispersion coefficient tensor [L^2T^{-1}]; v is the flow velocity vector [LT^{-1}]
 87 derived from the solution of the flow model; q_s represents volumetric flow rate per unit
 88 volume of aquifer associated with a fluid source or sink [T^{-1}] and C_s is the concentration of
 89 the source or sink [ML^{-3}].

90 The flow equation is solved using MODFLOW (McDonald and Harbaugh, 1988), and the
 91 transport equation is solved using MT3DS (Zheng and Wang, 1999).

92 2.2. The Ensemble Kalman Filter

93 The ensemble Kalman filter was first introduced by Evensen (2003) to circumvent the
 94 difficulty of propagating covariances in time in the original and extended Kalman filter
 95 formulations. The restart EnKF (r-EnKF) has proven its capacity for contaminant source
 96 identification in synthetic cases (Xu and Gómez-Hernández, 2016b, 2018); now, we propose
 97 to test the r-EnKF in a sandbox experiment. For this specific case, there will be eight
 98 parameters to identify, six related to the contaminant source, and two related to aquifer
 99 geometry. In the first group, they are the contaminant source location (X_s, Z_s), the injection
 100 concentration I_c , the injection rate I_r , plus the starting T_s and ending T_e release times. In
 101 the second group, the algorithm will try to identify the position along the x direction X_b
 102 and the total depth Z_b of a vertical plate inserted about the center of the sandbox to deflect
 103 the flowlines. The rest of the parameters defining the flow and transport conditions in the
 104 sandbox are not subject to identification and are equal to their observed values as explained

105 in the description of the experiment in the next section. The r-EnKF is shortly described
106 next.

107 In the ensemble Kalman filter with extended state vector, we deal with two types of
108 variables, the system parameters subject of identification, of which there could be observa-
109 tions or not, and the state of the system, of which there will be observations. The state
110 is forecasted in time solving the corresponding state equations, with the latest parameter
111 update, up to the specific time steps when observations are collected; these observations are
112 assimilated by the filter and serve to update the parameters and the state of the system. In
113 the restart filter, state variables are not updated, only system parameters are, because the
114 system state forecast for the next observation time is restarted from time zero to make sure
115 that the forecasted system state is fully coherent with the state equations, and, in our case,
116 with the updated contaminant source. (In the original implementation of the filter, both
117 state and parameters are updated, and the state system is forecasted from the last updated
118 state values using the last updated parameters.) The r-EnKF is an iterative algorithm that
119 cycles forecast and data assimilation (with the corresponding parameter update) until all
120 observations have been accounted for. The implementation of the r-EnKF for the identifica-
121 tion of the eight parameters described above can be summarized as follows (Evensen, 2003;
122 Xu and Gómez-Hernández, 2016b):

- 123 1. Generate an initial ensemble of parameter values. An ensemble of N_e realizations
124 of eight-tuples of the parameters to be identified is generated. Parameter values are
125 drawn, independently, from uniform distributions defined between first-guess minimum
126 and maximum values—there are no restrictions on these uniform distributions, their
127 range can be wider or narrower than the one used in this paper, and they do not have
128 to necessarily contain the “real” value, they are simply used to initialize the algorithm.
129 We build N_e vectors S_i with the eight parameters for each realization:

$$S_i = [Xs_i, Zs_i, Xb_i, Zb_i, Ic_i, Ir_i, Ts_i, Te_i]^T \quad (3)$$

130 where i is the realization index and the superscript T stands for transpose.

- 131 2. Repeat for each system state observation time. Forecast the state. For each ensemble
 132 member, forecast the system state, that is, the concentrations in the aquifer, for the
 133 t^{th} observation time using the values of the parameters from the last update (or the
 134 initial parameters for the first observation time). In the original implementation of
 135 the EnKF, the system state at the t^{th} observation time is forecasted based on the
 136 concentrations at the $(t-1)^{th}$ observation time and using the last updated parameters;
 137 however, it is virtually impossible to account for an update of the source location or
 138 the injection time unless the state equation is solved from time zero, thus the need to
 139 restart the simulation from time zero (Xu and Gómez-Hernández, 2016b). The forecast
 140 of concentrations is given by

$$C_i^f(t) = \psi [C_0, S_i^a(t-1)], \quad (4)$$

141 where the superscripts f and a refer to forecasted and updated values after assimilation,
 142 respectively; ψ represents the numerical model that forecast, in time, concentrations,
 143 on a grid with N_m nodes; C_i is an $N_m \times 1$ column vector containing the forecasted
 144 concentrations at all the discretization nodes of the numerical model for realization
 145 i ; S_i^a is the vector with the last updated parameters; C_0 is the initial contaminant
 146 concentration of the domain, which is the same for all realizations. The forecast of the
 147 parameters is simply

$$S_i^f(t) = S_i^a(t-1). \quad (5)$$

- 148 3. Parameters update. First compute the parameter covariance through the ensemble of
 149 forecasted realizations

$$P_S^f(t) = \frac{1}{N_e} \sum_{i=1}^{N_e} \left\{ \left[S_i^f(t) - \overline{S_i^f(t)} \right] \left[S_i^f(t) - \overline{S_i^f(t)} \right]^T \right\} \quad (6)$$

150 with

$$\overline{S_i^f(t)} = \frac{1}{N_e} \sum_{i=1}^{N_e} S_i^f(t), \quad (7)$$

151 where P_S^f is an 8×8 matrix of parameter covariances and $\overline{S_i^f(t)}$ is an 8×1 column vector
 152 of parameter averages. Then, compute the parameter-concentration cross-covariances
 153 but only with the forecasted concentration values that fall at concentration observation
 154 locations for time t (for the sake of simplicity, we will assume that observations are
 155 taken coinciding with some of the numerical model nodes, if not, there will be a need to
 156 provide a linear averaging procedure to estimate concentrations at observation locations
 157 from model concentration forecasts)

$$P_{SC}^f(t) = \frac{1}{N_e} \sum_{i=1}^{N_e} \left\{ \left[S_i^f(t) - \overline{S_i^f(t)} \right] \left[C_i^f(t) - \overline{C_i^f(t)} \right]^T \right\} \quad (8)$$

158 with

$$\overline{C_i^f(t)} = \frac{1}{N_e} \sum_{i=1}^{N_e} C_i^f(t), \quad (9)$$

159 where P_{SC}^f is an $8 \times N_o$ matrix of parameter-concentration cross-covariances, with N_o
 160 being the number of nodes of the numerical model at which observations are taken at
 161 time step t , and $\overline{C_i^f(t)}$ is an $N_o \times 1$ column vector of average concentrations. Next,
 162 compute the $8 \times N_o$ Kalman gain matrix $K(t)$ as

$$K(t) = P_S^f(t) [P_{SC}^f(t) + R(t)]^{-1} \quad (10)$$

163 where $R(t)$ is an $N_o \times N_o$ diagonal observation error covariance matrix (implying that
 164 there is no correlation between observation errors and proceed to update the parameter
 165 values, realization by realization by

$$S_i^a(t) = S_i^f(t) + K(t) \left[d_i(t) - C_{io}^f(t) \right], \quad (11)$$

166 where $d_i(t)$ is an $N_o \times 1$ vector of observed concentrations (including observation errors
167 with covariance given by $R(t)$) and $C_{io}^f(t)$ is an $N_o \times 1$ vector of forecasted concentra-
168 tions.

169 4. Go back to step 2 and repeat the whole process until all observations are assimilated.

170 3. Experimental Case

171 3.1. Description of the experiment

172 A single point pollution experiment was performed in a sandbox using sodium fluorescein
173 as tracer. The sandbox is built in plexiglass and has external dimensions of 120 cm \times 14
174 cm \times 70 cm as sketched in Fig. 1. The internal volume of 96 cm \times 10 cm \times 70 cm is
175 filled with constant-diameter spherical glass beads. There are two reservoirs at the edges of
176 the box imposing constant water levels of 60.7 cm and 53.6 m upstream and downstream,
177 respectively. An injector was set up at the upstream part of the sandbox at the location
178 indicated by a red square in the figure, and a plastic plate was vertically inserted inside
179 the glass beads in the middle of the sandbox, whose position and length is also shown in
180 the figure. The experimental equipment was placed in a dark box and a digital camera was
181 used to capture, every 5 s, the fluorescein luminosity within the rectangular zone of 85 cm
182 by 44 cm marked with a ticked rectangle in Fig. 1. The pictures were then processed and
183 the fluorescein luminosity transformed into concentrations after a calibration procedure, as
184 described by Citarella et al. (2015). In this case, eight different fluorescein concentrations
185 ($C = 0; 2.5; 5; 10; 20; 25; 30; 35$ mg/l) were used to calibrate and generate the luminosity-
186 concentration curves in each picture pixel. The total experiment time lasted 1965 s, the
187 injection started at time 120 s and finished at time 1000 s. During the experiment, the rate
188 and concentration of the injection were also recorded.

189 It is very important to note that there are no piezometric head observations. The design
190 of the tank did not allow for those observations. Had there been piezometric head data, they

191 could have been assimilated in the filter and, without doubt, would have helped in improving
192 the identification (as shown by Xu and Gómez-Hernández (2018)).

193 *3.2. Numerical Model*

194 Since the thickness of the sandbox along the y axis is relatively small, we can assume
195 that the variability of piezometric heads and concentration along this direction is negligible.
196 Therefore, a two-dimensional groundwater flow and transport model in the XZ plane is
197 built. The upstream and downstream vertical boundaries are set as constant prescribed
198 piezometric head values, and the bottom boundary is impermeable while the top boundary
199 is the phreatic surface. The model corresponds to the yellowish area in Fig. 1, where
200 the coordinates of the four model corners are given. The tank is filled with homogeneous
201 spherical glass beads with a conductivity of 0.58 cm/s and a porosity of 0.37. The vertical
202 plastic plate was inserted at a distance of 52 cm from the left boundary and its length is of
203 42 cm. It is modeled as an impermeable barrier, which will deflect the flowlines towards the
204 bottom of the sandbox. The sandbox is discretized into 96 columns, one row, and 70 layers;
205 the size of each cell is $(\Delta x, \Delta y, \Delta z) = (1, 10, 1)$ cm. The total simulation time is 1800 s and
206 is discretized into 90 uniform time steps. Citarella et al. (2015) evaluated the longitudinal
207 and transverse dispersivities of the spherical beads, resulting in values of 0.16 cm and 0.048
208 cm, respectively. The flow and transport parameters are collected in Table 1.

209 The release happens at coordinates (18.5 cm, 30.5 cm), with a concentration of 20 mg/l
210 and an injection rate of 0.95 cm³/s. To start the ensemble Kalman filter 800 8-tuples of
211 the source and plate parameters are generated from uniform distributions (not centered at
212 the true values). The true values of the parameters to identify and the suspect range of the
213 uniform distributions used to generate the initial ensemble are collected in Table 2.

214 4. Application

215 The objective of this work is to demonstrate the capacity of the r-EnKF for the identifi-
216 cation of contaminant source information, including contaminant source location (X_s, Z_s) ,
217 injection information (I_c, I_r) and release time (T_s, T_e) together with the position and length
218 of the vertical plate (X_b, Z_b) , using concentration observations collected in a laboratory ex-
219 periment. As a prior test, we analyze a synthetic case, in which the concentration data are
220 generated by the numerical model of the sandbox, therefore removing any modeling error
221 since the forward model used to forecast by the r-EnKF will coincide with the model used to
222 generate the observations. In the next section, we will redo the analysis using the laboratory
223 data, we will analyze the problems found and propose some solutions.

224 4.1. Synthetic Sandbox Test

225 In this case, we design two scenarios $(S1, S2)$ with different number of observation wells
226 to evaluate the performance of the r-EnKF: scenario $S1$ with 20 observation wells, and
227 scenario $S2$ with 24 observation wells containing 4 additional wells ($\#21, \#22, \#23, \#24$)
228 located at the four corners of the suspect release area (see Fig. 1). The rationale for the
229 second scenario is that, after analyzing the first scenario, we felt that additional information
230 about the plume evolution was needed, and thus we decided to add four wells around the
231 suspect release zone. Such an addition will, indeed, improve the characterization. In both
232 scenarios, model error is neglected and we assume that observation errors are uncorrelated
233 with mean zero, and standard deviation of 0.1 mg/l.

234 Figure 2 and 3 show the time evolution of the ensemble mean and the ensemble variance,
235 respectively, of the updated state parameters for the two scenarios. Figure 4 shows the
236 evolution in time of the boxplots computed from the 800 ensemble members. After time
237 step 60, the convergence rate of the means and variances of the parameters are less than 1%
238 and 5%, respectively, all the parameters get close to the final estimation and become stable.
239 Notice also the sudden drop of the variance at a given time step for most of the parameters.

240 This drop is related to the activation of new observation wells as time progresses, what
241 implies that the amount of information assimilated by the filter does not vary continuously
242 in time, but rather it increases stepwise, with steps occurring when new wells observe, for
243 the first time, the arrival of the solute plume. We can distinguish between the parameters
244 that are perfectly identified by an ensemble mean equal to the true value, and practically
245 zero variance, and those that are approximated closely but which are not exact and present
246 some residual uncertainty. In the first group, there are the position parameters for the plate,
247 Xb and Zb , plus the vertical location of the release source Zs , independently of whether 20
248 or 24 data are used during the assimilation steps; in the second group are the remaining
249 parameters, which become more precise (mean closer to the true value) and less uncertain
250 (smaller variability) for $S2$ than for $S1$. The horizontal source location Xs is less sensitive
251 to the concentration data, and only when the four additional data points in the corners of
252 the suspect release location are added the algorithm is able to provide a good estimate for
253 this parameter; similar comment can be made about the beginning Ts and end Te times
254 of the release. The injection concentration Ic and injection rate Ir are well identified by
255 their median values, with smallest uncertainty for $S2$. These results are consistent with
256 the sensitivity of concentrations at the observation locations to changes in the parameter
257 values: concentration distributions are most sensitive to the position of the plate, which
258 affects the flow field, and the vertical release location, which affects the main trajectory of
259 the contaminant plume, but are less sensitive to the other parameters, for which variations
260 within the identified uncertainty ranges induce concentration changes of the same order of
261 magnitude as the observation errors. Also notice that the horizontal coordinate of the release
262 and the starting and ending release times are correlated for the purpose of identifying their
263 values (a displacement of the horizontal coordinate of the release could be compensated with
264 a displacement of its starting time), what also explains their larger uncertainties.

265 These results prove that the r-EnKF could work for the identification of a contaminant
266 source and of some parameters defining the geometry of the aquifer. The next step is to test

267 the algorithm under more realistic conditions using observations obtained from a laboratory
268 experiment.

269 4.2. Laboratory Sandbox Test

270 The sandbox experiment was carried out as described previously. Figure 5 shows a
271 picture of the fluorescein plume at the 48th time step (840 s since the beginning of the
272 release) already transformed into concentration values and the position of the observation
273 points. The deflection of the flowlines induced by the vertical plate is clearly seen. Notice
274 that only a few observation piezometers will actually detect the plume breakthrough. Before
275 testing the r-EnKF, we performed a simulation of the concentration evolution using the
276 known release parameters and compared the predictions with the observed data. Figure
277 6 shows a comparison between observed and numerically predicted concentrations at five
278 observation locations (wells #7, #9, #10, #13, #22) through which the plume passes. As
279 can be seen, the reproduction is very good for the closest well #22, and it deteriorates with
280 the distance from the source, but not dramatically, except for well #9. For this well, the
281 beginning and ending times of the breakthrough curve are the same for predictions and
282 observations, but the mismatch in concentrations indicates either some error in the model
283 parameters or faulty observations. The predicted breakthrough curve in the farthest well,
284 though, is quite close to the observed one. In the application that follows we will analyze
285 different observation error distributions in an attempt to identify the source parameters by
286 the r-EnKF.

287 We have run the r-EnKF with three different magnitudes of the observation error, which
288 will be referred to as $R1$, $R2$, and $R3$. In all three cases, the error mean is zero and its
289 standard deviation is 0.5 mg/l for $R1$, 1.0 mg/l for $R2$, and 3.0 mg/l for $R3$. We must
290 notice that in previous experiments, Cupola et al. (2015a) report an observation error with
291 a standard deviation around 1 mg/l.

292 The hydraulic conductivity value of the beads, which is considered homogeneous in each

293 realization, is considered uncertain and drawn from a Gaussian distribution with a mean
294 of 0.58 cm/s and a standard deviation of 0.05 cm/s. We have decided to introduce some
295 uncertainty on the beads hydraulic conductivity as a surrogate to model error. The choice of
296 a Gaussian distribution centered at the calibrated conductivity value was arbitrary, any other
297 distribution could have been used. Considering that the differences in the results between
298 including or not such an uncertainty are minimal (and not reported here), we believe that
299 the choice of the specific distribution has little effect in the final outcome.

300 Fig. 7 shows the boxplots of the updated parameters at different time steps for the three
301 scenarios *R1*, *R2*, and *R3*. The results are not as good as for the synthetic case, for which the
302 observed concentrations were generated with the same numerical model used for the forecast
303 step in the Kalman filter. The first thing to note is that for scenario *R1*, the use of a small
304 observation error makes the r-EnKF to seek for source parameter values that can be far
305 from the true ones in order to produce concentrations that are close to the observed values,
306 and, particularly, the injection concentration and injection rate do not seem to converge to
307 a stable value after 90 time steps. The other parameters do reach a stable median, not as
308 close to the true values as for the synthetic case but close enough except for the horizontal
309 position of the vertical plate.

310 When the observation error is increased (scenario *R2*), the two main findings are that the
311 two injection parameters now seem to reach a stable estimate (albeit with large uncertainty)
312 with a median close to the true value, and that all parameters have a wider uncertainty range.
313 The median estimate of the initial and ending release times is also closer to the true ones
314 than in *R1*. The horizontal position of the vertical plate continues to be underestimated, as
315 well as the length of the plate.

316 When the observation error is increased even more (scenario *R3*) the main effect is that
317 the final estimates have wide uncertainty estimates, and for some of the parameters it seems
318 as if the concentration observations do not bring any added value since the boxplot width
319 remains unaltered through the assimilation steps. The estimates of the parameters by their

320 median is comparable to the results in *R2*, but their uncertainty is larger.

321 The predicted concentrations at three observation wells that were not used during the
322 assimilation step computed using the initial 8-tuples of parameters, and using the 8-tuples
323 obtained at the end of the three scenarios are shown in Figure 8. The figure shows the
324 true concentrations in the sandbox as a dotted blue line, each one of the 800 predicted
325 concentration breakthrough curves computed with the 8-tuples of the ensemble, along with
326 their median, as a red line, and their 90% confidence interval, as dashed lines. It can be
327 observed that, prior to assimilation (top row), concentration predictions were very scattered,
328 and that after the assimilation (bottom three rows, one for each scenario) the breakthrough
329 curves change substantially (compare, for instance, the median curves). For scenario *R1*, the
330 scatter of prediction curves is the smallest but recall that these wells were not used during
331 the assimilation, the updated parameters were biased because the algorithm tried to fit the
332 observed concentrations too closely and as a result, at the control wells, the prediction of
333 the true curves by the ensemble median is also biased, up to the point that the true curves
334 are outside the 90% confidence interval. For scenarios *R2* and *R3* the median curves for the
335 three wells have a smaller bias than for *R1*, and the main difference between *R2* and *R3* is
336 the same as for parameter prediction, the uncertainty is the widest for *R3*. The true curve
337 is in both cases within the 90% confidence interval of the predictions.

338 At this point, it seems that an observation error with a standard deviation of 1 mg/l was
339 the most consistent with our observations and model. As mentioned above, this conclusion
340 fits the findings by Cupola et al. (2015a). Yet, we were concerned with the big discrepancy
341 between predictions and observations at well #9, so we decided to rerun scenario *R2* without
342 using the data from this well. The results for this scenario, called *R2b*, are shown in Figure
343 9. When comparing this figure to the middle two rows in Figure 7 we can notice that there
344 is some overall improvement in the estimation of the true parameters —particularly for the
345 position parameters— by the median values of the ensemble without a significant change
346 on their uncertainty. This improvement reinforces our suspicion that there could have been

347 some problems in the data collection at well #9.

348 We also considered that there could be a problem with the tightness of the vertical
349 plate after its insertion in the sandbox. The plate was supposed to represent a perfectly
350 impermeable barrier, and no evidence of the contrary was observed during the experiments,
351 yet the contact between the plate and sandbox walls could have had some small gaps, making
352 the plate slightly permeable. Therefore, we decided to rerun scenario *R2* but assuming that
353 the plate is slightly permeable, more precisely, with a conductivity of two orders of magnitude
354 smaller than the beads, this value was chosen arbitrarily low since nothing was actually
355 observed in the laboratory. The results for the new scenario, referred to as *R2c* are shown in
356 Figure 10. (Note that well #9 was kept in this scenario.) The main difference of this run is
357 that the estimate of the size of the vertical plate by the median of the ensemble jumps from
358 40.5 cm to 44.2 cm (true value is 42.0 cm) indicating that possibly the plate conductivity
359 used in this scenario was too large and, as a consequence, the algorithm enlarges the plate
360 to reproduce the observed concentrations. This result, while does not serve to justify that
361 the tightness of the plate explains the numerical model misfit, shows the impact that such
362 permeability would have in the estimation of the remaining parameters defining the plate.

363 We can conclude that the r-EnKF can be applied to a more realistic case of a homogeneous
364 aquifer in a sandbox for the identification of a contaminant source and some geometry
365 parameters. A proper evaluation of the observation errors is paramount, since attempting
366 to match too closely the data may result in biased estimates of the parameters.

367 5. Summary and Conclusion

368 The main purpose of this paper was to test whether the restart ensemble Kalman filter,
369 which had been successfully applied in synthetic experiments, could be applied to a more
370 realistic case based on a sandbox experiment. The test focuses on the identification of the
371 parameters defining a finite-pulse point injection of a solute, together with the position of a
372 vertical plate that modifies the initial rectangular geometry of the sandbox.

373 As a preliminary step, we tested the r-EnKF in a synthetic case mimicking the sandbox.
374 Under these very controlled conditions, the algorithm performs well, as expected. The main
375 difference with previous synthetic analyses is that no piezometric head data were used during
376 the assimilation step of the filter.

377 Then, the r-EnKF is tested using the data coming from the laboratory experiment. In this
378 case, the observations were not generated by a computer code nor we knew the observation
379 error magnitude. The analysis of the results show that using a too small observation error
380 variance results in more or less precise but biased estimates, both for the parameters subject
381 to identification and for the concentrations at control locations. When a larger observation
382 error (with a standard deviation of 1 mg/l) is introduced, estimates and predictions improve,
383 although with larger uncertainty. And finally, when the observation error is large, the results
384 worsen considerably. The removal of a suspicious observation well, the concentration of which
385 is always underestimated by our forecast model, improves the results, indicating that the
386 measurements from such well may need to be reconsidered. The changes observed after
387 making the vertical plate slightly permeable do not appear to justify the hypothesis that the
388 plate leaks.

389 The r-EnKF appears as a good algorithm for source identification in aquifers, yet it still
390 needs further tests in closer-to-reality conditions. Currently, the sandbox has been replaced
391 with a heterogeneous distribution of glass beads, and the challenge is to test the method in
392 this new sandbox.

393 **Acknowledgements** Financial support to carry out this work was received from the
394 Spanish Ministry of Economy and Competitiveness through project CGL2014-59841-P, and
395 from the Spanish Ministry of Education, Culture and Sports through a fellowship for the
396 mobility of professors in foreign research and higher education institutions to the second
397 author, reference PRX17/00150. The authors also would like to thank Università degli
398 Studi di Parma for providing the experimental equipment and data.

399 **References**

- 400 Atmadja, J., Bagtzoglou, A.C., 2001. State of the Art Report on Mathematical Methods for
401 Groundwater Pollution Source Identification. *Environmental Forensics* 2, 205–214.
- 402 Ayvaz, M.T., 2010. A linked simulation-optimization model for solving the unknown ground-
403 water pollution source identification problems. *Journal of Contaminant Hydrology* 117,
404 46–59.
- 405 Bagtzoglou, A.C., Atmadja, J., 2005. Mathematical Methods for Hydrologic Inversion: The
406 Case of Pollution Source Identification. *Water Pollution* 5, 65–96.
- 407 Bagtzoglou, A.C., Dougherty, D.E., Tompson, A.F.B., 1992. Application of particle methods
408 to reliable identification of groundwater pollution sources. *Water Resources Management*
409 6, 15–23.
- 410 Butera, I., Tanda, M.G., Zanini, A., 2013. Simultaneous identification of the pollutant release
411 history and the source location in groundwater by means of a geostatistical approach.
412 *Stochastic Environmental Research and Risk Assessment* 27, 1269–1280.
- 413 Chen, Y., Zhang, D., 2006. Data assimilation for transient flow in geologic formations via
414 ensemble Kalman filter. *Advances in Water Resources* 29, 1107–1122.
- 415 Citarella, D., Cupola, F., Tanda, M.G., Zanini, A., 2015. Evaluation of dispersivity coeffi-
416 cients by means of a laboratory image analysis. *Journal of Contaminant Hydrology* 172,
417 10–23.
- 418 Cupola, F., Tanda, M.G., Zanini, A., 2015a. Contaminant release history identification in
419 2-d heterogeneous aquifers through a minimum relative entropy approach. *SpringerPlus*
420 4, 656.

- 421 Cupola, F., Tanda, M.G., Zanini, A., 2015b. Laboratory sandbox validation of pollutant
422 source location methods. *Stochastic Environmental Research and Risk Assessment* 29,
423 169–182.
- 424 Evensen, G., 2003. The Ensemble Kalman Filter: Theoretical formulation and practical
425 implementation. *Ocean Dynamics* 53, 343–367.
- 426 Gorelick, S.M., Evans, B., Remson, I., 1983. Identifying sources of groundwater pollution:
427 An optimization approach. *Water Resources Research* 19, 779–790.
- 428 Houtekamer, P.L., Mitchell, H.L., 2001. A Sequential Ensemble Kalman Filter for Atmo-
429 spheric Data Assimilation. 0203058.
- 430 Koch, J., Nowak, W., 2016. Identification of contaminant source architectures - A statisti-
431 cal inversion that emulates multiphase physics in a computationally practicable manner.
432 *Water Resources Research* 52, 1009–1025. 2014WR016527.
- 433 Li, L., Zhou, H., Gómez-Hernández, J.J., Hendricks Franssen, H.J., 2012a. Jointly map-
434 ping hydraulic conductivity and porosity by assimilating concentration data via ensemble
435 Kalman filter. *Journal of Hydrology* 428-429, 152–169.
- 436 Li, L., Zhou, H., Hendricks Franssen, H.J., Gómez-Hernández, J.J., 2012b. Groundwater flow
437 inverse modeling in non-MultiGaussian media: Performance assessment of the normal-
438 score Ensemble Kalman Filter. *Hydrology and Earth System Sciences* 16, 573–590.
- 439 Liu, C., Ball, W.P., 1999. Application of inverse methods to contaminant source identification
440 from aquitard diffusion profiles at dover afb, delaware. *Water Resources Research* 35,
441 1975–1985.
- 442 Mahar, P.S., Datta, B., 2000. Identification of Pollution Sources in Transient Groundwater
443 Systems. *Water Resources Management* 14, 209–227.

444 McDonald, J.M., Harbaugh, A.W., 1988. A modular three-dimensional finite-difference flow
445 model. *Techniques of Water Resources Investigations of the U.S. Geological Survey, Book*
446 *6*, 586.

447 Michalak, A.M., 2003. A method for enforcing parameter nonnegativity in Bayesian in-
448 verse problems with an application to contaminant source identification. *Water Resources*
449 *Research* 39, 1–14.

450 Michalak, A.M., Kitanidis, P.K., 2004. Estimation of historical groundwater contaminant
451 distribution using the adjoint state method applied to geostatistical inverse modeling.
452 *Water Resources Research* 40.

453 Neupauer, R.M., Wilson, J.L., 1999. Adjoint method for obtaining backward-in-time location
454 and travel time probabilities of a conservative groundwater contaminant. *Water Resources*
455 *Research* 35, 3389–3398.

456 Sun, A.Y., Painter, S.L., Wittmeyer, G.W., 2006. A constrained robust least squares ap-
457 proach for contaminant release history identification. *Water Resources Research* 42, 1–13.

458 Wagner, B.J., 1992. Simultaneous parameter estimation and contaminant source character-
459 ization for coupled groundwater flow and contaminant transport modelling. *Journal of*
460 *Hydrology* 135, 275–303.

461 Woodbury, A., Sudicky, E., Ulrych, T.J., Ludwig, R., 1998. Three-dimensional plume source
462 reconstruction using minimum relative entropy inversion. *Journal of Contaminant Hydrol-*
463 *ogy* 32, 131–158.

464 Woodbury, A.D., Ulrych, T.J., 1996. Minimum relative entropy inversion: Theory and ap-
465 plication to recovering the release history of a groundwater contaminant. *Water Resources*
466 *Research* 32, 2671–2681.

- 467 Xu, T., Gómez-Hernández, J.J., 2015. Inverse sequential simulation: A new approach for the
468 characterization of hydraulic conductivities demonstrated on a non-Gaussian field. *Water*
469 *Resources Research* 51, 2227–2242. 2014WR016527.
- 470 Xu, T., Gómez-Hernández, J.J., 2016a. Characterization of non-Gaussian conductivities and
471 porosities with hydraulic heads, solute concentrations, and water temperatures. *Water*
472 *Resources Research* 52, 6111–6136.
- 473 Xu, T., Gómez-Hernández, J.J., 2016b. Joint identification of contaminant source location,
474 initial release time, and initial solute concentration in an aquifer via ensemble Kalman
475 filtering. *Water Resources Research* .
- 476 Xu, T., Gómez-Hernández, J.J., 2018. Simultaneous identification of a contaminant source
477 and hydraulic conductivity via the restart normal-score ensemble Kalman filter. *Advances*
478 *in Water Resources* 112, 106–123.
- 479 Xu, T., Gómez-Hernández, J.J., Zhou, H., Li, L., 2013a. The power of transient piezometric
480 head data in inverse modeling: An application of the localized normal-score EnKF with
481 covariance inflation in a heterogenous bimodal hydraulic conductivity field. *Advances in*
482 *Water Resources* 54, 100–118.
- 483 Xu, T., Jaime Gómez-Hernández, J., Li, L., Zhou, H., 2013b. Parallelized ensemble Kalman
484 filter for hydraulic conductivity characterization. *Computers and Geosciences* 52, 42–49.
- 485 Yeh, H.D., Chang, T.H., Lin, Y.C., 2007. Groundwater contaminant source identification
486 by a hybrid heuristic approach. *Water Resources Research* 43, 1–16.
- 487 Zanini, A., Woodbury, A.D., 2016. Contaminant source reconstruction by empirical Bayes
488 and Akaike’s Bayesian Information Criterion. *Journal of Contaminant Hydrology* 185-186,
489 74–86.

- 490 Zheng, C., Wang, P.P., 1999. MT3DMS: A Modular Three-Dimensional Multispecies Trans-
491 port Model , 219.
- 492 Zhou, H., Gómez-Hernández, J.J., Hendricks Franssen, H.J., Li, L., 2011. An approach to
493 handling non-Gaussianity of parameters and state variables in ensemble Kalman filtering.
494 Advances in Water Resources 34, 844–864.
- 495 Zhou, H., Gómez-Hernández, J.J., Li, L., 2014. Inverse methods in hydrogeology: Evolution
496 and recent trends. Advances in Water Resources 63, 22–37.

Table 1: Parameters of the groundwater flow and transport model

Hydr. conduct., K	0.58 cm/s
Porosity, ϕ	0.37
Long. disp., α_L	0.16 cm
Transv. disp., α_T	0.048 cm

Table 2: Source and geometry parameters. True values and suspect ranges for the generation of the initial ensemble of realizations

Parameter	Actual Value	Suspect Range
X_s (cm) - x -coordinate of source	18.5	16 – 25
Z_s (cm) - z -coordinate of source	30.5	23 – 32
X_b (cm) - x -coordinate of plate	52.5	50 – 59
Z_b (cm) - plate length	42.5	35 – 43
I_r (cm ³ /s) - injection rate	0.95	0.6 – 1.1
I_c (mg/l) - injection load	20	5 – 24
T_s (s) - starting release time	120	80 – 260
T_e (s) - ending release time	1000	960 – 1140

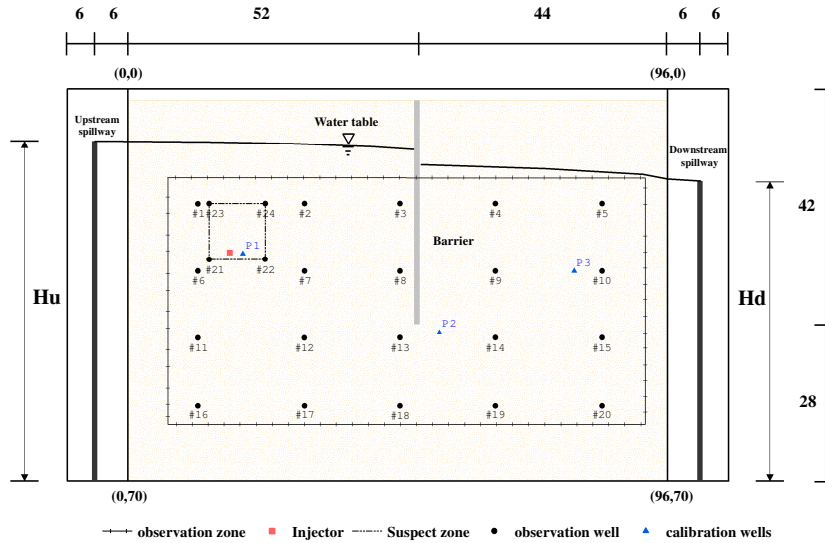


Figure 1: Sketch of the experimental device with indication of the upstream (H_u) and downstream (H_d) constant head boundaries. The ticked rectangle corresponds to the area captured by the camera in which concentrations will be monitored. Red dot is the release location. Dashed line around red dot indicates the release suspect location. Dimensions are in cm. Coordinates of the four corners of the flow and transport models are also shown.

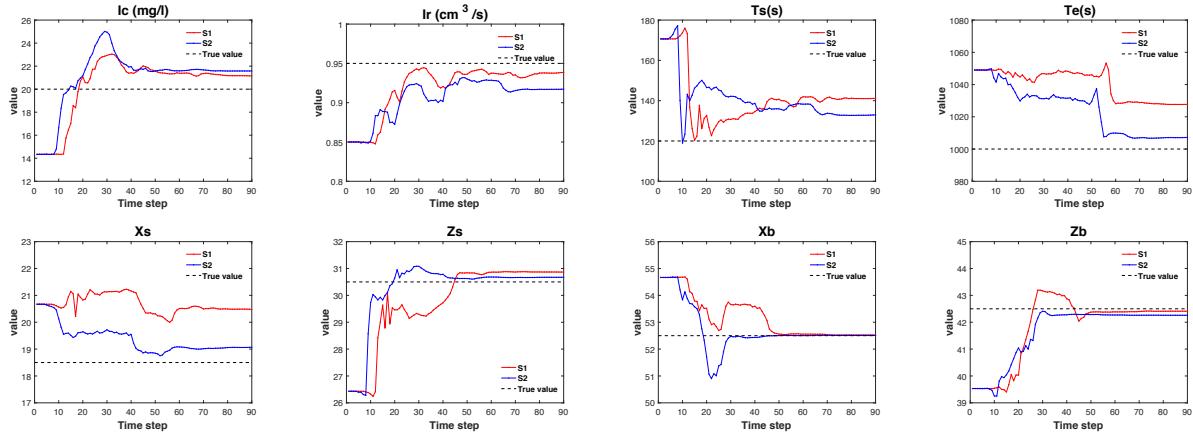


Figure 2: Time evolution of the ensemble mean of the 8 updated parameters, contaminant source location (X_s , Z_s), plate position (X_b , Z_b), injection information (I_c , I_r) and release time interval (T_s , T_e) for scenarios S_1 and S_2

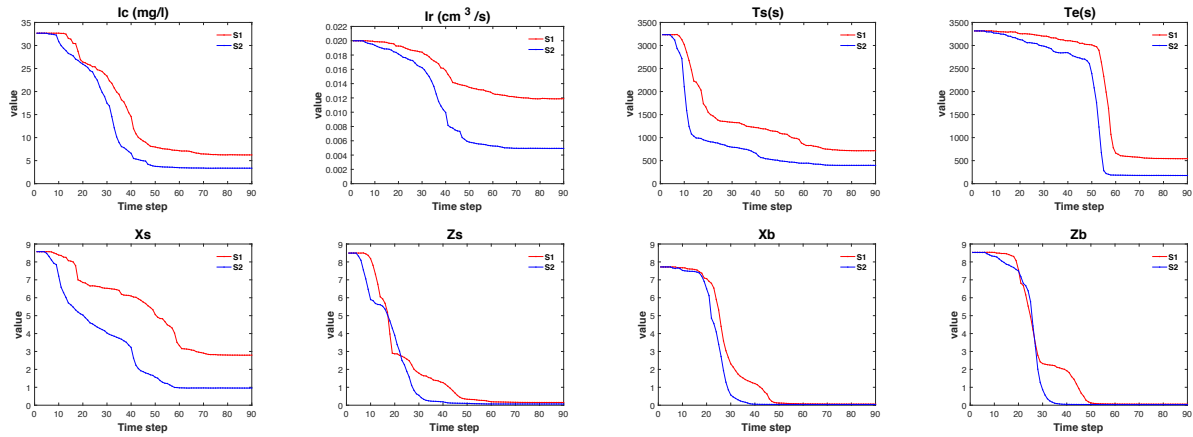


Figure 3: Time evolution of the ensemble variance for the same parameters and scenarios as in the previous figure.

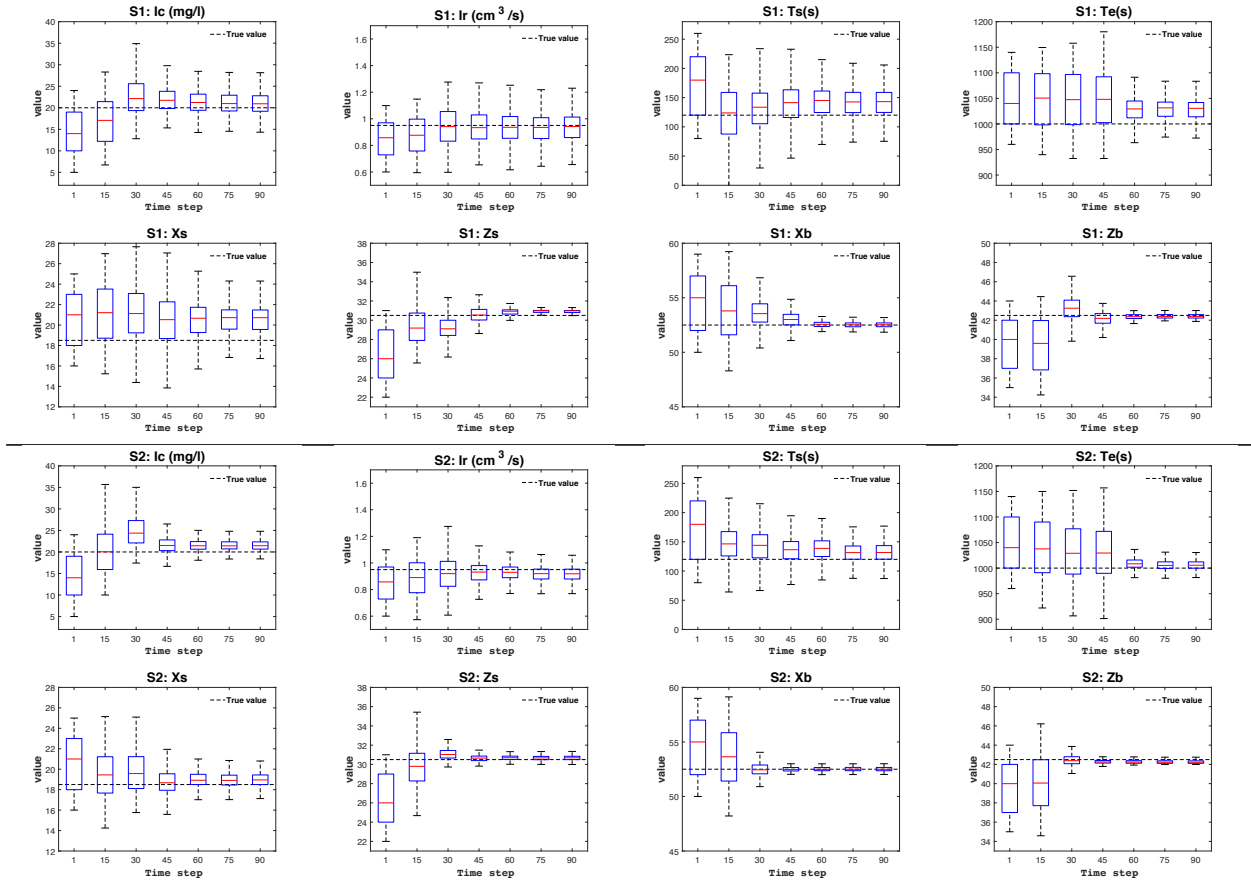


Figure 4: Boxplot of the 8 updated parameters at different time steps (1, 15, 30, 45, 60, 75, 90) for scenarios S1 and S2

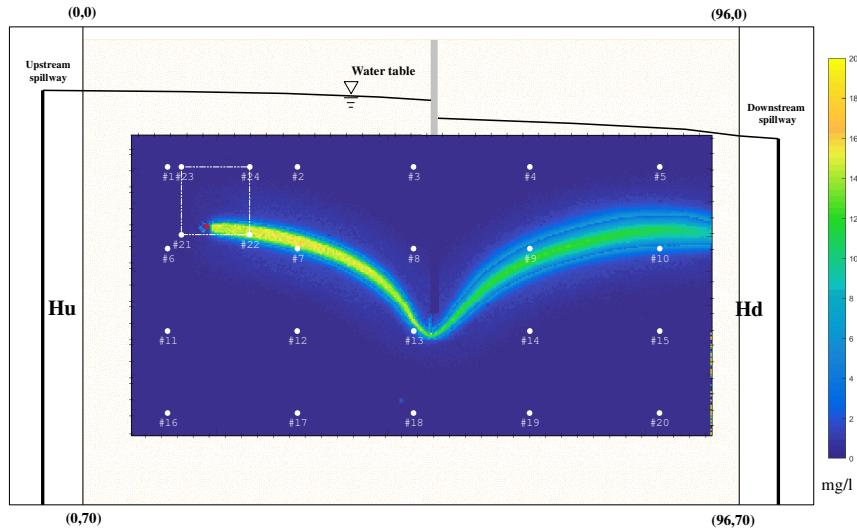


Figure 5: Fluorescein concentration field in the sandbox at the 48th time step. The area shown corresponds to the observation zone indicated in Fig. 1. The dash line shows the suspect zone for the injection and the white dots indicate the observation wells.

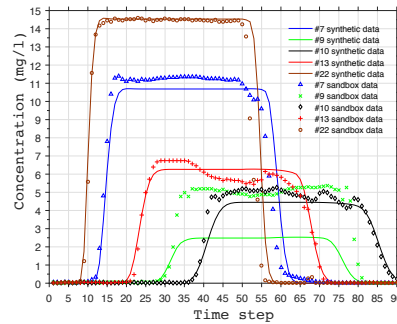


Figure 6: Fluorescein observed breakthrough curves at the observation wells located inside the plume and the curves computed from the numerical model

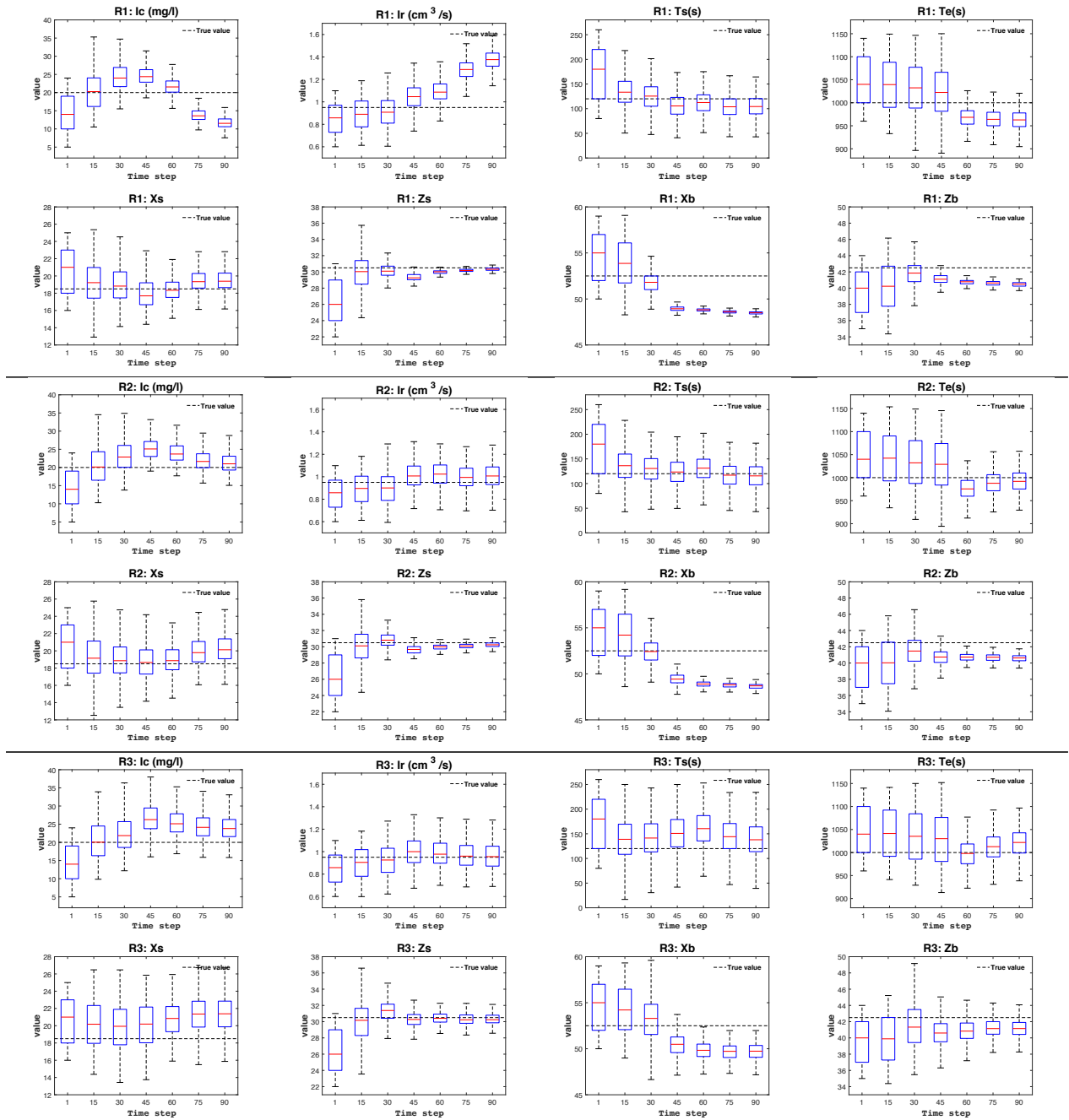


Figure 7: Boxplot of of the 8 updated parameters at time steps 1, 15, 30, 45, 60, 75 and 90 for scenarios $R1$, $R2$ and $R3$

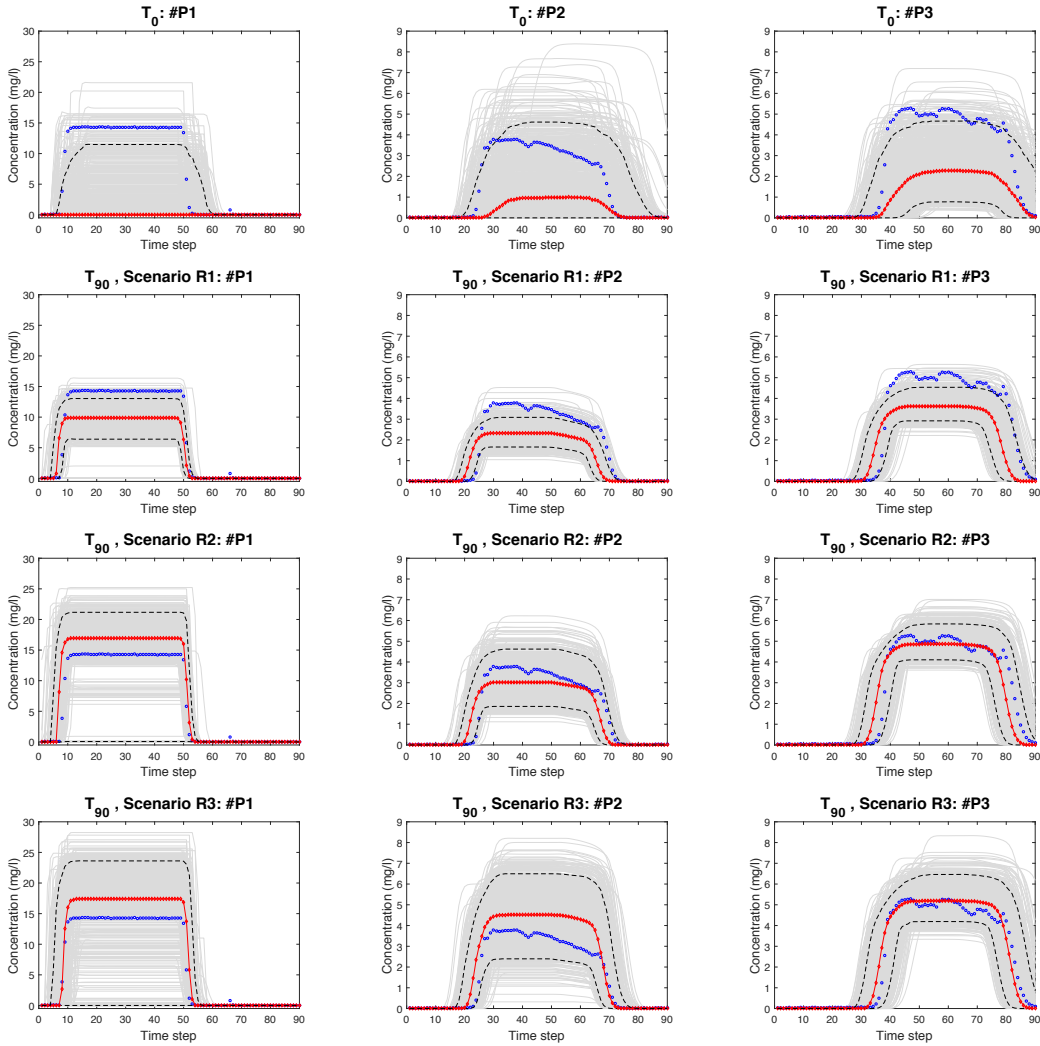


Figure 8: Breakthrough curves at control wells. The blue dots correspond to the curves in the sandbox experiment. The thin gray lines are the curves for all 800 realizations; they are summarized by their median (red diamond lines) and their 5 and 95 percentiles (black dash lines).

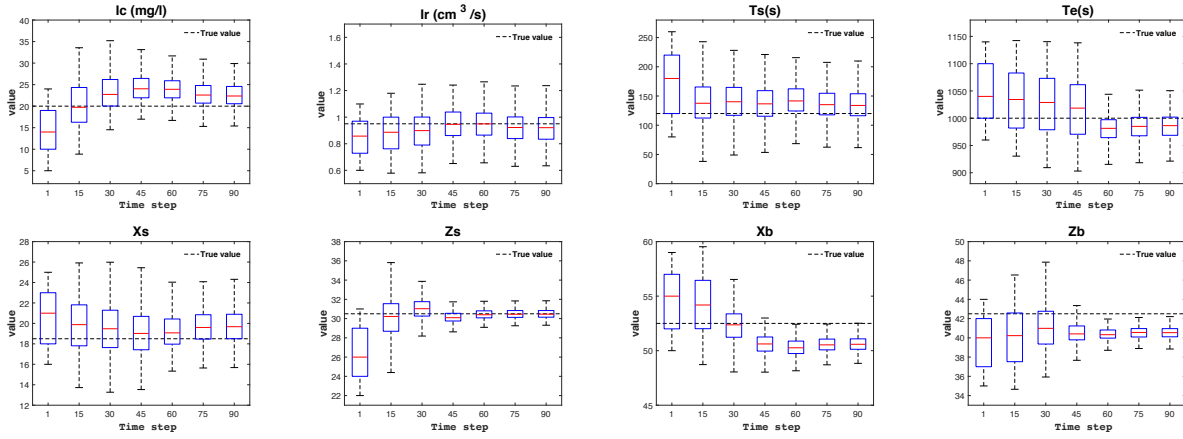


Figure 9: Boxplot of the 8 updated parameters in scenario *R2b* at different time steps (1, 15, 30, 45, 60, 75, 90)

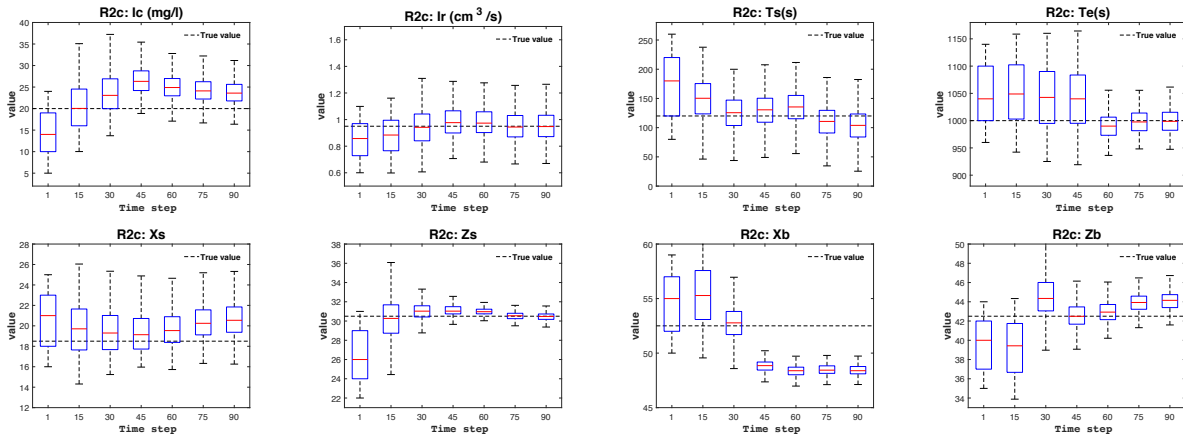


Figure 10: Boxplot of the 8 updated parameters in scenario *R2c* at different time steps (1, 15, 30, 45, 60, 75, 90)

LaTeX Source Files

[Click here to download LaTeX Source Files: Latex source file.zip](#)